Chapter 7
Applications and Examples

7.1 Contaminant Plume Sizes Associated to Different Active Solids

There are several situations of practical interest, both in nature and in manmade processes, in which there is fluid flow through a bed of inert particles, packed around a solid mass that contacts with the moving fluid. Examples may be found in diverse fields, such as dilute catalyst fixed bed reactors, fluidized bed combustion, ore leaching and water contamination by buried waste. In such processes there is an interplay between diffusion, convection and dispersion and a detailed systematic study of the problem has been given by Coelho and Guedes de Carvalho [16] for transfer from buried flat surfaces and for transfer from buried spheres. Both these references present accurate solutions for certain limiting situations, namely those of low and high fluid velocity (more precisely, low and high Peclet numbers).

When the mass transfer process occurs in a porous media with a fluid flowing around the soluble particle, and at low fluid velocities (as typically observed in underground flow), the assumption of thin boundary layer is not legitimate, and the theoretical analysis developed by Coelho and Guedes de Carvalho [16] is not applicable. Therefore, it is necessary to employ numerical methods for a correct analysis of the mass transfer process in more general situations.

Flow around a buried sphere is an important model situation in many processes and in a recent work Guedes de Carvalho et al. [31] treated the problem numerically, so as to cover the entire range of values of Peclet and Schmidt numbers.

Flow along buried cylindrical surfaces and flat surfaces are also important model situations, and were investigated theoretically and numerically by Alves et al. [8], yielding results for a wide range of values of Peclet number, aspect ratio of soluble solid mass and Schmidt number.

Over the last years, our focus has been driven preferentially to the analysis of the mass transfer of particles with spherical geometry. This work is a contribution

F. A. Coutelieris and J. M. P. Q. Delgado, *Transport Processes in Porous Media*, Advanced Structured Materials 20, DOI: 10.1007/978-3-642-27910-2_7,

for the study of mass transfer of soluble particles with different geometries buried in inert particles with smaller diameter. Additionally, a simple approximate method is presented to obtain concentration contours plots for solute distribution around and downstream of the buried surfaces (with different geometries).

The following sections present a detailed description of the mass transfer and dispersion process around a soluble solid particle with different shapes (sphere, cylinder or a plane surface aligned with the flow, cylinder in cross-flow, prolate spheroid and a oblate spheroid) buried in a packed bed of smaller inert particles with uniform voidage, with a moving fluid with constant interstitial velocity.

7.1.1 Concentration Profiles From a Soluble Flat Slab

In many processes, both in industry and in the environment, there is a physical/chemical interaction between a lump of solid matter buried in a granular bed of small inert particles, and the fluid flowing around it, through the interstices in the bed. In such processes, a region of higher solute/reactant concentration develops in the immediate vicinity of the "active mass", with consequent solute migration away from it, by diffusion and convection in the moving fluid.

In groundwater flow applications the velocities are low and small values of Peclet number are therefore observed; solute dispersion is then determined by molecular diffusion.

The concentration distribution in the wake of a soluble solid particle immersed in a granular bed of inert particles, through which fluid flows with "uniform velocity", has been obtained, for solute transport by both advection and diffusion. General expressions, based in a theoretical analysis and using the expressions obtained for the mass transfer rate, n, are presented to estimate contaminant "plume" sizes downstream of the polluting source.

In this model situation, we only consider the steady state conditions when the plane surface releases solute to the flowing liquid at a constant rate, n. The value of n depends on the concentration gradients next to the surface of the plane surface and these depend on the process variables. According to Eq. 6.68, the following equation

$$n = \frac{D'_{\mathrm{m}}}{L}\,\varepsilon\, bL\,(c^* - c_0)\left[\frac{2}{\pi}\mathrm{Pe}'^{\,1/4}_{\mathrm{sf}} + \frac{4}{\pi}\mathrm{Pe}'_{\mathrm{sf}}\right]^{1/2} \tag{7.1}$$

gives n within 3% of the exact value, over the entire range of values of $\mathrm{Pe}'_{\mathrm{sf}}$, if $\mathrm{Pe}'_{\mathrm{p}} < 0.1$.

Imagine a situation of continuous injection of solute, at a rate n, at the point $(x = 0,\, y = 0)$, in the porous medium through which fluid flows with uniform interstitial velocity u_0. It is assumed that the volume of additional fluid injected into the main fluid, with the solute, is negligible.

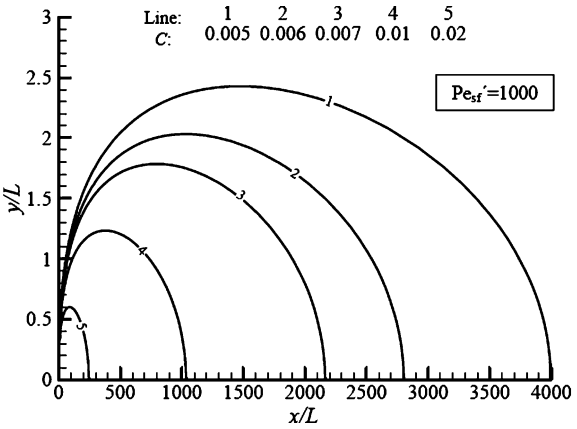

Fig. 7.1 Concentration profiles obtained with Eq. 7.3, at long distances from the flat slab

Making $D_T \cong D_L \cong D'_m$ a diffusion/convection cloud is again formed and the corresponding concentration contour plots are given by the solution for the "continuous point source" [100] of two-dimensional solute transport,

$$c = \frac{n/b}{2\varepsilon\pi D'_m} \exp\left[\frac{u_0 x}{2D'_m}\right] K_0\left\{\sqrt{\frac{u_0^2(x^2+y^2)}{4D'^2_m}}\right\} \tag{7.2}$$

where b is the depth and K_0 is the modified Bessel function of second kind and zero order. In our case, the problem of mass transfer from a soluble slab (with length L) immersed in a granular bed of inerts through which fluid flow with uniform interstitial velocity and with n from Eq. 7.1, one obtains after re-arrangement:

$$C = \frac{\sqrt{\frac{2}{\pi}\mathrm{Pe}'^{1/4}_{sf} + \frac{4}{\pi}\mathrm{Pe}'_{sf}}}{2\pi} \exp\left[\frac{\mathrm{Pe}'_{sf}}{2}\frac{x}{L}\right] K_0\left\{\sqrt{\frac{\mathrm{Pe}'^2_{sf}}{4}\left[\left(\frac{x}{L}\right)^2 + \left(\frac{y}{L}\right)^2\right]}\right\} \tag{7.3}$$

This equation may be used to estimate the region of propagation of a given concentration level.

Figure 7.1 show the concentration contour plots obtained, taking $\mathrm{Pe}' = 1,000$ as an example, for low values of C. As the value of C decreases, the distance of the contour surfaces to the solid soluble particle increase and the solution for the "continuous point source" approach to the "exact" solution, obtained numerically. This result was confirmed by Gurdes de Carvalho et al. [31], who analysed the accuracy of the "continuous point source" solution, for different ranges of C, in the case of an active sphere immersed in a packed bed. The authors showed that for the higher values of C the concentration contours obtained with "continuous point source" solution deviates considerably from the "exact" solution, obtained numerically. However, for low values of C and if a correct value of n is used, true coincidence is observed between the numerical results and the "continuous point source" solution.

7.1.2 Concentration Profiles From a Cylinder Aligned With Flow

The analytical solution for a continuous point source has also been derived by Wexler [100], solving the three-dimensional solute-transport equation from a point source. The solution is given by

$$c = \frac{n}{4\varepsilon\pi(x^2+y^2)^{1/2}D'_{\mathrm{m}}}\exp\left[\frac{u_0[x-(x^2+y^2)^{1/2}]}{2D'_{\mathrm{m}}}\right]. \tag{7.4}$$

with $D_{\mathrm{T}} \cong D_{\mathrm{L}} \cong D'_{\mathrm{m}}$ and a good estimate for n is required. The point source is located at the point $(x, y) = (0, 0)$. In our case, the problem of mass transfer around a soluble cylinder (with length L and diameter d_1) immersed in a granular bed of inerts through which fluid flow with uniform interstitial velocity, the mass flux rate is expressed as,

$$n = \varepsilon k\pi d_1 L(c^* - c_0) = \mathrm{Sh}_{\mathrm{c}}^{'}\frac{D'_{\mathrm{m}}}{\mathrm{L}}\varepsilon\pi d_1 L(c^* - c_0) \tag{7.5}$$

with Sherwood number, $\mathrm{Sh}_{\mathrm{c}}^{'}$, given by Eq. 6.73. Making use of the dimensionless variables (please see Eq. 6.58), Eq. 7.4 results, after re-arrangement:

$$C = \frac{\sqrt{\frac{2}{\pi}\mathrm{Pe}_{\mathrm{c}}'^{1/4} + \frac{4}{\pi}\mathrm{Pe}'_{\mathrm{c}} + \left(6\frac{L}{d_1}\right)^{1/2} + \left(\frac{4}{3}\frac{L}{d_1}\right)^{3/2} + \frac{5}{3}\mathrm{Pe}_{\mathrm{c}}'^{5/9}\left(\frac{L}{d_1}\right) - \mathrm{Pe}_{\mathrm{c}}'^{2/9}\left(2\frac{L}{d_1}\right)^{1/3}}}{4(L/d_1)\left[(x/L)^2+(y/L)^2\right]^{1/2}}$$
$$\times \exp\left\{\frac{\mathrm{Pe}'_{\mathrm{c}}}{2}\left[x/L - \left[(x/L)^2+(y/L)^2+\right]^{1/2}\right]\right\} \tag{7.6}$$

Figure 7.2 show the concentration contour plots obtained, taking $\mathrm{Pe}'_{\mathrm{c}} = 1,000$, as an example, for low values of C.

7.1.3 Concentration Profiles From a Soluble Sphere

In this model situation, we investigate the steady state conditions when a soluble sphere releases solute to the flowing fluid, with uniform interstitial velocity u_0, at a constant rate, n. Again, it is assumed that the volume of additional fluid injected into the main fluid, with the solute, is negligible.

A diffusion/convection cloud is formed and the corresponding concentration contour plots for the "continuous point source", at the point $(x = 0, y = 0)$, are also given by Eq. 7.4. If n from Eq. 6.82 is substituted in Eq. 7.4, the resulting equation may be re-arranged to read

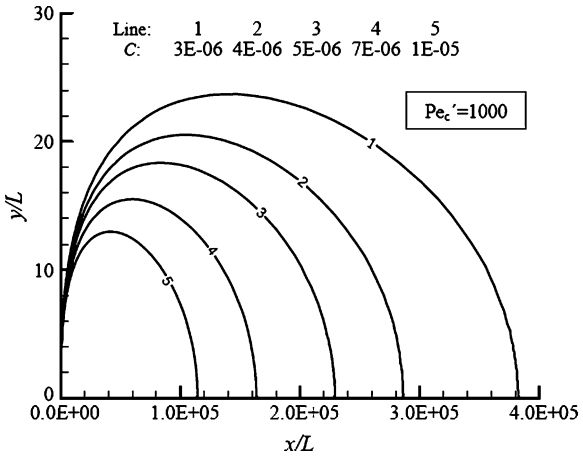

Fig. 7.2 Concentration profiles obtained with Eq. 7.6, at long distances from the cylinder

$$C = \frac{\left[4 + \frac{4}{5}\mathrm{Pe}_s'^{\,2/3} + \frac{4}{\pi}\mathrm{Pe}_s'\right]^{1/2}}{2\left[(x/a)^2 + (y/a)^2\right]^{1/2}} \exp\left\{\frac{\mathrm{Pe}_s'}{4}\left[(x/a) - \left[(x/a)^2 + (y/a)^2\right]^{1/2}\right]\right\} \tag{7.7}$$

Figure 7.3 show the concentration contour plots obtained, taking $\mathrm{Pe}_s' = 1,000$, as an example, for low values of C.

7.1.4 Concentration Profiles From a Cylinder in Cross Flow

If a slightly soluble cylinder, buried in a packed bed, is exposed to uniform fluid flow with velocity u_0, it will then release solute at a rate n, given by Eq. 6.91.

A diffusion/convection cloud is formed and the corresponding concentration contour plots for the "continuous point source", at the point $(x = 0, y = 0)$, are also given by Eq. 7.4, and the substitution of n/b from Eq. 6.91 into 7.4 gives then

$$C = \frac{\left[\frac{2}{\pi^2}\mathrm{Pe}_{cf}'^{\,1/4} + \frac{32}{\pi^3}\mathrm{Pe}_{cf}'\right]^{1/2}}{2} \exp\left[\frac{\mathrm{Pe}_{cf}'}{4}\frac{x}{a}\right] \times K_0\left\{\sqrt{\frac{\mathrm{Pe}_{cf}'^{\,2}}{16}\left[\left(\frac{x}{a}\right)^2 + \left(\frac{y}{a}\right)^2\right]}\right\} \tag{7.8}$$

Concentration contours given by Eq. 7.8 are shown in Fig. 7.4, for $\mathrm{Pe}_{cf}' = 1,000$ (note that for $d_1 = 2$ m, $u_0 = 5 \times 10^{-4}$ mm/s and $D_m' \cong 10^{-9}$ m^2/s, there results $\mathrm{Pe}_{cf}' \cong 1,000$). From a detailed study of a similar nature, for flow past a sphere, it is reasonable to expect that values of the downstream reach of each contour surface (defined as the value of x/a, for $y/a = 0$, for that surface),

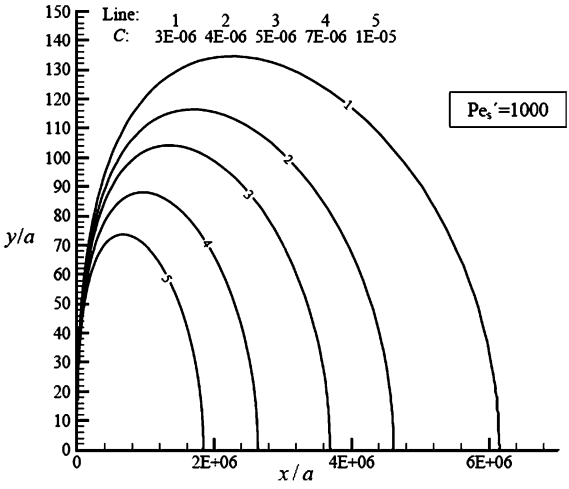

Fig. 7.3 Concentration profiles obtained with Eq. 7.7, at long distances from the sphere

predicted by Eq. 7.8, will differ by less than 10% from the exact value, if $\mathrm{Pe}' > 500$ and $C < 0.05$. The accuracy of the prediction will improve as C is decreased.

7.1.5 Concentration Profiles From a Prolate Spheroid

If a soluble prolate spheroid, buried in a packed bed, is exposed to uniform fluid flow with uniform interstitial velocity u_0, it will then release solute at a rate n, given by

$$n_{\mathrm{T}} = \varepsilon D'_{\mathrm{m}} \sqrt{\frac{4}{\pi}\mathrm{Pe}'_{\mathrm{ps}}} \left(\frac{2}{3} \frac{e^3}{e - (1-e^2)\tanh^{-1} e} \right)^{1/2} \frac{2\pi a}{(1-e^2)^{1/6}} (C^* - C_0) \qquad (7.9)$$

with Sherwood number, $\mathrm{Sh}'_{\mathrm{ps}}$, given by Eq. 6.115. Making use of the dimensionless variables, Eq. 7.4 results, after re-arrangement:

$$\frac{C - C_0}{C^* - C_0} = \frac{\frac{1}{2}\left[\frac{4}{\pi}\mathrm{Pe}'_{\mathrm{ps}}\right]^{1/2} \left(\frac{2}{3} \frac{e^3}{e - (1-e^2)\tanh^{-1} e} \right)^{1/2}}{4\left[(x/d_{\mathrm{eq}})^2 + (y/d_{\mathrm{eq}})^2\right]^{1/2}} \times \exp\left\{ \frac{\mathrm{Pe}'_{\mathrm{ps}}}{2} \left[x/d_{\mathrm{eq}} - \left[(x/d_{\mathrm{eq}})^2 + (y/d_{\mathrm{eq}})^2\right]^{1/2} \right] \right\} \qquad (7.10)$$

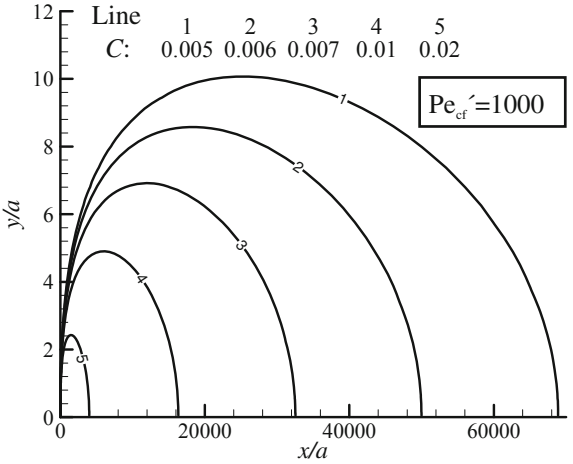

Fig. 7.4 Concentration profiles obtained with Eq. 7.8, at long distances from the cylinder in cross flow

7.1.6 Concentration Profiles From an Oblate Spheroid

If a slightly oblate spheroid, buried in a packed bed, is exposed to uniform fluid flow with uniform interstitial velocity u_0, it will then release solute at a rate n, given by

$$n_T = \varepsilon D'_m \sqrt{\frac{4}{\pi}\mathrm{Pe}'} \left(\frac{4}{3} \frac{e^3}{-e + e^3 + \sqrt{1-e^2}\cot^{-1}\left(\sqrt{1/e^2-1}\right)} \right)^{1/2} \times \frac{2\pi a^2 (1-e^2)^{1/3}}{d_{eq}} (C^* - C_0) \tag{7.11}$$

with Sherwood number, Sh'_{os}, given by Eq. 6.129. Making use of the dimensionless variables, Eq. 7.4 results, after re-arrangement:

$$\frac{C - C_0}{C* - C_0} = \frac{\frac{1}{2}\left[\frac{4}{\pi}\mathrm{Pe}'_{os}\right]^{1/2} \left(\frac{4}{3} \frac{e^3}{-e + e^3 + \sqrt{1-e^2}\cot^{-1}\left(\sqrt{1/e^2-1}\right)} \right)^{1/2}}{4\left[(x/d_{eq})^2 + (y/d_{eq})^2\right]^{1/2}} \times \exp\left\{ \frac{\mathrm{Pe}'_{os}}{2} \left[x/d_{eq} - \left[(x/d_{eq})^2 + (y/d_{eq})^2\right]^{1/2} \right] \right\} \tag{7.12}$$

Figure 7.5 show the concentration contour plots obtained, taking $\mathrm{Pe}'_{os} = 1,000$ and $e = 0.5$ as an example, for low values of concentration, C. As the value of C decreases, the distance of the contour surfaces to the solid soluble particle increase and the solution for the "continuous point source" approach to the "exact" solution, possible to obtain numerically (i.e. if a correct value of n is used, true coincidence is observed).

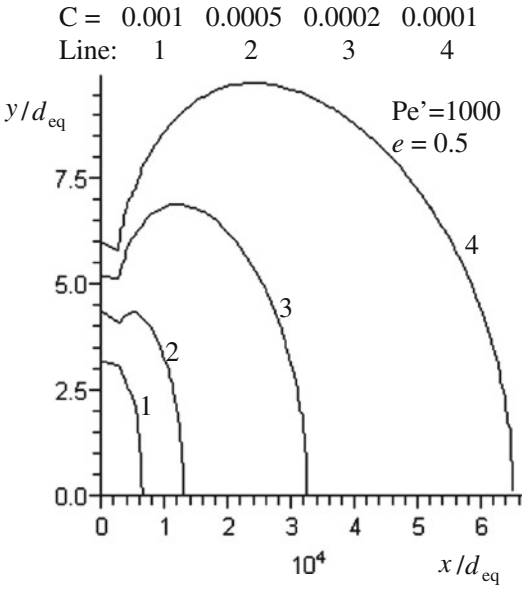

Fig. 7.5 Concentration profiles obtained with Eq. 7.12, at long distances from the oblate spheroid

The problem of mass transfer between a buried solid with different shapes and the fluid flowing along it in a granular bed, lends itself to a simple full theoretical analysis, under an appropriate set of conditions.

The elliptic partial differential equations resulting from a differential mass balance have been solved numerically over a wide range of values of the relevant parameters. It was found that the resulting Sherwood values are in good agreement with experimental results.

Results of the exact numerical solutions and analytical solutions were also used to predict the solute migration from an active solid particle buried in a packed bed of inert particles, through which fluid flows with uniform velocity. The concentration contour surfaces were obtained using an analytical solution of continuous injection of solute at a point source in a uniform stream and the proposed correlations for the mass transfer rate developed numerically or analytically.

7.2 Rising Damp in Building Walls

Rising damp, a world-wide phenomenon, is a major cause of decay in masonry materials such as stone, brick and mortar. The conservation of historic buildings has become important nowadays and has developed significantly in recent years. Rising damp in historic buildings may be considered one of the most important of all the different manifestations of dampness, leading to the destruction of stone materials due to frost/defrost cycles and the presence of salts associated with crystallization (Künzel [61] argues that in many cases increased salt content is

interpreted as rising damp), decay in elements in contact with stone walls, such as wooden beams, wooden ceilings and other finishings, and insanitary conditions caused by excess humidity associated with the development of fungus and mould.

Rising damp, which originates in the ground and permeates porous materials by capillarity, is one of the main causes of decay in old buildings, particularly those containing thick walls built from different materials. Having identified the particular characteristics of those buildings, it is important to recognize the limitations of traditional technologies and to investigate new solutions for the phenomenon. The traditional techniques used to deal with this kind of problem (such as watertight barriers, the injection of hydrofuge products, etc.) sometimes prove ineffective or are very expensive, justifying the need to find new approaches (see [34]).

The Building Physics Laboratory (LFC), at the University of Porto-Faculty of Engineering (FEUP) has been developing important experimental research into the problems of rising damp. In recent years the principles for a treatment technique called the "Wall Base Ventilation System to Treat Rising Damp–HUMIVENT device" has been validated and characterised in experiments. The technique consists of circulating air around the base of very thick walls built from different materials, with a relative humidity saturation distance. Wall base ventilation increases evaporation, which reduces the level of the damp front. This is possible only when the groundwater is lower than the base of the wall [17].

In previous research it was observed that the "wall base ventilation device" reduces the level of the wet front. Following this, a series of experiments were carried out to explore boundary conditions, geometry, engine speed, etc., and it was possible to observe that a hygro-regulated system is essential in controlling possible condensation inside the system. A hygro-regulated system is a mechanical system controlled by probes placed at the inlet and at the outlet. In accordance with pre-programmed criteria, the probes will switch the system on/off.

7.2.1 Rising Damp Theory

The phenomenon of rising damp can be analysed using the sharp front model developed by Hall and Hoff [39]. This model describes the relationship between sorptivity, S, wall thickness, b, evaporation potential, e, and capillary rise heights, h.

Considering the absorption inflow and evaporation loss to be balanced and disregarding gravitational forces (see Fig. 7.6), the following differential equation is obtained [40]

$$b\frac{di}{dt} = b\frac{S}{2}t^{-1/2} - eh \tag{7.13}$$

where i is the volume of liquid absorbed per unit cross section in time t [36]. Considering that $i = \theta_w h$, the following expression is obtained

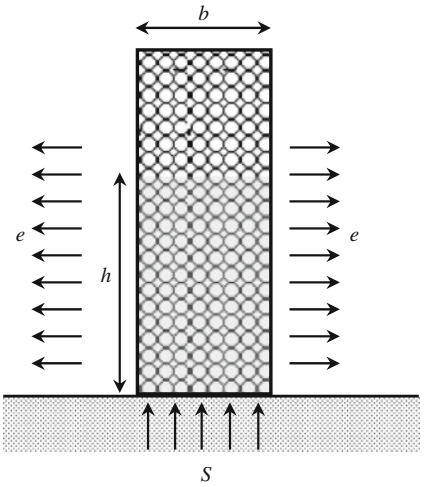

Fig. 7.6 Sketch of sharp front model

$$\frac{dh}{dt} = \frac{S}{2\theta_w} t^{-1/2} - \frac{eh}{b\theta_w} \tag{7.14}$$

with $i = St^{1/2} = \theta_w h$, results

$$\frac{dh}{dt} = \frac{S^2}{2\theta_w^2} \frac{1}{h} - \frac{eh}{b\theta_w} \tag{7.15}$$

The analytical solution of Eq. 7.15 is

$$h = S\sqrt{\frac{b}{2e\theta_w}\left[1 - \exp\left(-\frac{2e}{b\theta_w}t\right)\right]} \tag{7.16}$$

with the equilibrium height, h_∞, given by

$$h_\infty = S\sqrt{\frac{b}{2e\theta_w}} \tag{7.17}$$

7.2.2 The Wall Base Ventilation System

The wall base ventilation system (HUMIVENT device) consists of ventilating the base of walls using a natural ventilation process or by installing a hygro-regulated mechanical ventilation device (see Fig. 7.7). In terms of analysis, we considered a wall base ventilation system along which air is flowing close to the "saturated" wall $(0 < z < L)$.

In laminar flow, the transport of moisture and temperature across the boundary layers is controlled by molecular diffusion. The Reynolds number, Re, may be interpreted as the ratio of the flow of destabilising forces to stabilising forces

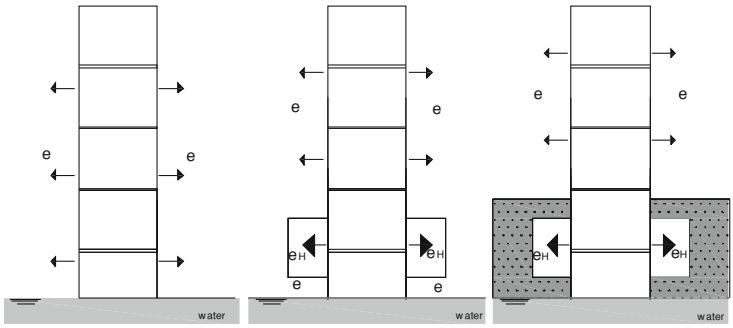

Fig. 7.7 Diagram of the different boundary conditions studied

(viscosity). Stable laminar flow is thus characterized by low Re values. Laminar flow occurs at Reynolds numbers of less than approximately 3×10^5. In our study $\mathrm{Re} < 10^5$, in all experiments.

If the analysis is restricted to situations in which the moisture transfer boundary layer is thin and if a small control volume is considered inside this boundary layer, with side lengths δz, δy and unity (perpendicular to the plane of the figure), a steady state material balance in the solute leads to

$$u\frac{\partial c}{\partial z} = D_{\mathrm{m}}\frac{\partial^2 c}{\partial y^2} + D_{\mathrm{m}}\frac{\partial^2 c}{\partial z^2} \tag{7.18}$$

where D_{m} is the molecular diffusion coefficient, in the cross stream and in the stream wise directions. If the boundary layer is thin compared to the length of the saturated wall, the last term on the right-hand side of Eq. 7.18 is likely to be negligible. For the situation outlined in Fig. 7.6, the boundary conditions are,

$$c = c_0 \quad z = 0 \quad y > 0 \tag{7.19a}$$

$$c = c^* \quad z > 0 \quad y = 0 \tag{7.19b}$$

$$c \to c_0 \quad z > 0 \quad y \to \infty \tag{7.19c}$$

and the analytical solution is given by [21]

$$\frac{c - c_0}{c^* - c_0} = \mathrm{erfc}\left(\frac{y}{2\sqrt{D_{\mathrm{m}} z/u}}\right) \tag{7.20}$$

where c_0 is the bulk concentration of water vapour, c^* is the equilibrium concentration of water vapour, and u is the air velocity. The flux of evaporation, N, at the saturated wall surface may be obtained from (7.20) as

$$N = -D_m \left(\frac{\partial c}{\partial y}\right)_{y=0} = (c^* - c_0)\left(\frac{D_m}{\pi z/u}\right)^{1/2} \tag{7.21}$$

Finally, it is possible to obtain the total rate of solid evaporation, n, over the whole wall surface

$$n = \int_0^L N\, h_{\mathrm{H}}\, dx = (c^* - c_0) h_{\mathrm{H}} L \left(\frac{4D_m}{\pi L/u}\right)^{1/2} \tag{7.22}$$

where $N = -D_m(\partial c/\partial y)_{y=0}$ and h_H is the width of HUMIVENT system.

If we consider a rising damp steady state, involving a wall buried in sand and a wall base ventilation system (HUMIVENT) located on both sides above the base (see Fig. 7.7), Eq. 7.17 produces

$$\frac{bS^2}{2\theta_{\mathrm{w}} h_\infty} = e(h_\infty - h_s - h_H) + e_H h_H + e_s h_s \tag{7.23}$$

with e_H (related to HUMIVENT) given by [34]

$$e_H = \frac{n}{L.h_H \rho_w} = \frac{(c^* - c_0)}{\rho_w}\left(\frac{4D_{\mathrm{m}}}{\pi L/u}\right)^{1/2} \tag{7.24}$$

and the steady-state height of rise given by

$$h_\infty = \left(1 - \frac{e_s}{e}\right)\frac{h_s}{2} + \left(1 - \frac{e_H}{e}\right)\frac{h_H}{2} + \sqrt{\frac{bS^2}{2\theta_{\mathrm{w}} e} + \left(\frac{e_s}{e} - 1\right)^2 \frac{h_s^2}{4} + \left(\frac{e_H}{e} - 1\right)^2 \frac{h_H^2}{4} + \left(1 - \frac{e_s}{e} - \frac{e_H}{e} + \frac{e_s e_H}{e2}\right)\frac{h_s h_H}{2}} \tag{7.25}$$

Noting that the evaporation potential related with sand placed on both sides of the wall above its base, e_s, will be negligible (sand water saturated) in comparison with the other evaporation rates, e and e_H, and Eq. 7.25 reduces then to

$$h_\infty = \frac{h_s}{2} + \left(1 - \frac{e_H}{e}\right)\frac{h_H}{2} + \sqrt{\frac{bS^2}{2\theta_{\mathrm{w}} e} + \frac{h_s^2}{4} + \left(\frac{e_H}{e} - 1\right)^2 \frac{h_H^2}{4} + \left(1 - \frac{e_H}{e}\right)\frac{h_s h_H}{2}} \tag{7.26}$$

and for $e_H = e_s = 0$, Eq. 7.26 reduces to

$$h_\infty = \frac{h_s}{2} + \frac{h_H}{2} + \sqrt{\frac{bS^2}{2\theta_{\mathrm{w}} e} + \frac{h_s^2}{4} + \frac{h_H^2}{4} + \frac{h_s h_H}{2}} \tag{7.27}$$

Finally, to estimate the evaporation potential, e, many existing formulae can be applied [53]. In this study we used the Penman–Monteith equation [34] which, given that the latitude of Porto is 40.15°, results in an evaporation potential of 0.0017 mm/min.

7.2.3 Numerical Simulation

The simulation programs to evaluate changes in the moisture content and temperature inside walls are essential instruments for simulating the wall's behaviour in the presence of moisture, depending on the internal and external climatic conditions [12].

The calculation program used in the numerical simulations for the experimental and analytical validations was WUFI-2D, developed by Fraunhofer Institute for Building Physics. The governing equation for moisture transport is [44]

$$\frac{dw}{d\phi}\frac{\partial\phi}{\partial t} = \nabla(D_{\varphi}\nabla\phi + \delta_{\mathrm{p}}\nabla\phi p_{\mathrm{s}}) \tag{7.28}$$

and the governing equation for heat transport is

$$\frac{dH}{dT}\frac{\partial T}{\partial t} = \nabla(\lambda_{\mathrm{T}}\nabla T) + h_{\mathrm{v}}\nabla(\delta_{\mathrm{p}}\nabla\varphi p_{\mathrm{s}}) \tag{7.29}$$

where dH/dT is the heat storage capacity of the moist building material, $dw/d\phi$ is the moisture storage capacity, λ_{T} is the thermal conductivity, D_{ϕ} is the liquid conduction coefficient, δ_{p} is the water vapour permeability, h_{v} is the evaporation enthalpy of the water, p_{s} is the water vapour saturation pressure, T is the temperature and ϕ is the relative humidity.

As hygrothermal modelling offers a powerful tool for predicting heat and moisture transport through multi-layer building assemblies. In this work, the hygrothermal model was used to compare the results of three case studies (monolithic wall) under different natural conditions (see Fig. 7.7). The laboratory climate was modelled by a sine wave varying between 19°C, 50% RH in winter and 21°C, 70% RH in summer, which corresponds to a normal moisture load (mean values of 60% RH and temperature of 20°C). The initial moisture content of the used materials was the equilibrium moisture at 80% RH. The simulation periods began on January 1.

The vapour diffusion thickness value used was zero (no coating) and the interior heat transfer coefficient was constant and equal to 8 W/m^{2}K. The exterior heat transfer coefficient only contained the convective part and was considered independent from the wind (constant value of 17 W/m^{2}K).

7.2.4 Rising Damp Analysis

7.2.4.1 In the Laboratory

The physical model selected consisted of a prismatic wall 1.58 m high, 2.00 m long and 0.20 m thick, waterproofed on the two upper sides (measuring

Table 7.1 Properties of the limestone sample [93]

		Limestone	
Bulk density, ρ (kg/m^3)		2155 ± 14	
Heat capacity, c_p (J/kgK)		1,000	
Porosity, ε (%)		19.7	
Thermal conductivity, λ_T (W/mK)		1.33 ± 0.025	
Vapor diffusion resistance factor, μ (−)	Dry cup:	41 ± 2.2	
	Wet cup:	29 ± 3.1	
Moisture storage function, w (kg/m^3)	HR (%)	*Adsorption*	*Desadsorption*
	4.0	0.521	0.951
	11.2	0.593	1.150
	34.8	0.872	1.239
	58.6	1.043	1.628
	76.3	1.237	2.360
	80.0	1.334	–
	84.2	1.584	–
	92.1	2.381	4.144
Capillary transport coefficient, D_w (m^2/s)	$w_{80\%} = 1.7$ kg/m^3	6.6×10^{-11}	
	$w_{sat} = 188$ kg/m^3	6.2×10^{-8}	
Water absorption coefficient, A (kg/m^{2}s$^{1/2}$)		0.024 ± 0.002	
Free-water saturation, w_f (kg/m^3)		177 ± 1.8	

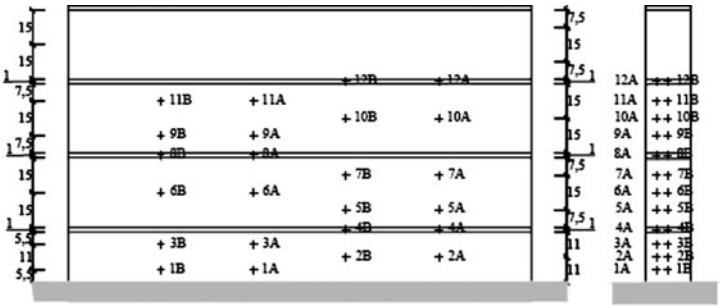

Fig. 7.8 Position of the relative humidity and temperature probes [93]

1.58 × 0.20 m^2) to prevent moisture entering from this direction. The limestone walls (see Table 7.1) were placed in a reservoir approximately 2.20 × 2.50 × 0.50 m^3 made from cement blocks. To assess moisture transfer inside the walls, probes were inserted at different heights and depths to measure relative humidity and temperature, as sketched in Fig. 7.8. These probes were then connected to a data acquisition and recording system.

The configurations tested are shown in Fig. 7.7. In Configuration 1 the base of the wall is immersed up to a height of 8 cm and, as we wished to assess the effect of the wall base ventilation system–HUMIVENT, in Configurations 2 and 3, a ventilation box was placed on both sides of the wall. The only difference between these configurations was that in Configuration 3 we measured the behaviour of a

Table 7.2 Experi ment values (average) for relative humidity and temperature inlet in the wal l and system outlet

Configuration 1	Configuration 2		Configuration 3	
ϕ_0 (%)	ϕ_0 (%)	ϕ_s (%)	ϕ_0 (%)	ϕ_s (%)
60.0	57.8	60.1	58.2	60.3
T_0 (°C)	T_0 (°C)	T_s (°C)	T_0 (°C)	T_s (°C)
20.0	22.6	22.4	23.0	22.8

Table 7.3 Comparison between experimental, analytical and numerical results (obtained with an error lesser than 5%)

h_∞ (mm)	Limestone		
	Conf. 1	Conf. 2	Conf. 3
Experiments	455–540	380–455	455–540
WUFI 2D (ϕ)	550	–	490
WUFI 2D (w)	520	–	490
Analytical solution	510	380	451
ϕ_{eq} (%)	60		
w_{eq} (kg/m^3)	1.047		

wall with both sides buried in sand to a height of 45 cm. The sand was saturated (100% RH) during the tests. To avoid turbulence, an air velocity of 0.083 m/s was used and the relative humidity and temperature values for the experiments are presented in Table 7.2.

The climatic conditions inside the laboratory during the experiments were considered constant at a temperature of 23°C and a relative humidity of 58%. Under these conditions and considering an air velocity inside the laboratory of 1 cm/s, the evaporation potential was given by [87]

$$e = D_m \frac{(c^* - c_0)}{\rho_w} 0.646 \frac{\mathrm{Re}^{1/2}\,\mathrm{Sc}^{1/3}}{L} \tag{7.30}$$

The resulting evaporation potential value is 0.46×10^{-4} mm/min. The evaporation potential associated with the HUMIVENT system, e_H, is given in Eq. 7.24 as 2.17×10^{-4} mm/min. If these values are inserted into Eq. 7.25, a steady state height of rise of 379.5 mm is obtained for Configuration 2 and a steady flow rate through the wall of about 27.1 L/year per metre length of wall. This value is very similar to the experimental results obtained, of between 380 and 455 mm (as sketched in Fig. 7.8, position 6 and 7–average value of 417.5 mm), and significantly different from the steady state height of rise obtained without the use of the HUMIVENT system, which was $h_\infty = 540$ mm in Configuration 1 (experimental value between 455 and 540 mm—Fig. 7.8, position 7 and 8—as shown in Table 7.3).

In the analyse of our experimental results, the following expression was used for water vapour diffusivity in air [56]

$$D_\mathrm{m}(m^2/s) = 2.23 \times 10^{-5} \left[\frac{273.15 + T(^\circ C)}{273.15}\right]^{1.5} \tag{7.31}$$

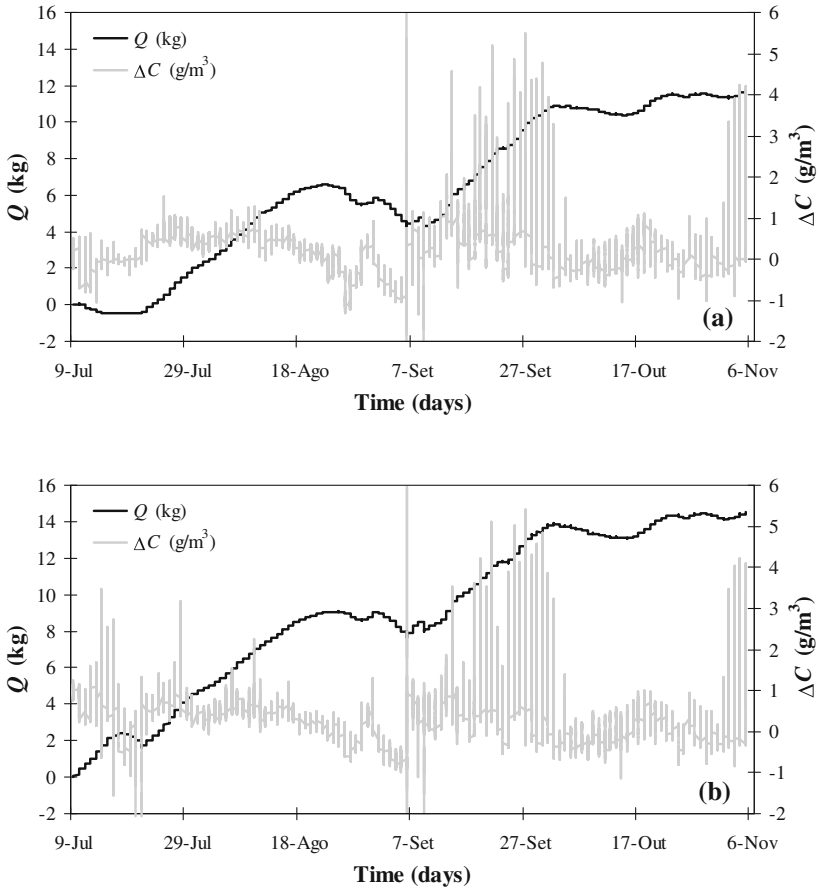

Fig. 7.9 Quantity of water vapour extracted and concentration differential (**a**) in Configuration 2 and (**b**) in Configuration 3

Table 7.3 shows the experimental results for the first series of laboratory tests, i.e. the rising damp values for the steady height of rise under different boundary conditions. The results of the experiment show that the presence of a wall base ventilation system on both sides prevents the damp front (see results) and that the simple analytical model proposed by Hall and Hoff [39] clearly describes the rising damp front when compared with the experiment results. During the four months of experimental research, in laboratory tests on Configurations 2 and 3 the new treatment technique extracted approximately 11.8 and 14.5 kg of water respectively (see Fig. 7.9a, b).

The simulation program provided the water content, the relative humidity and the temperature at all the points of the pre-defined grid and their evolution for the duration of the simulation. It also gave the heat and moisture flows along its

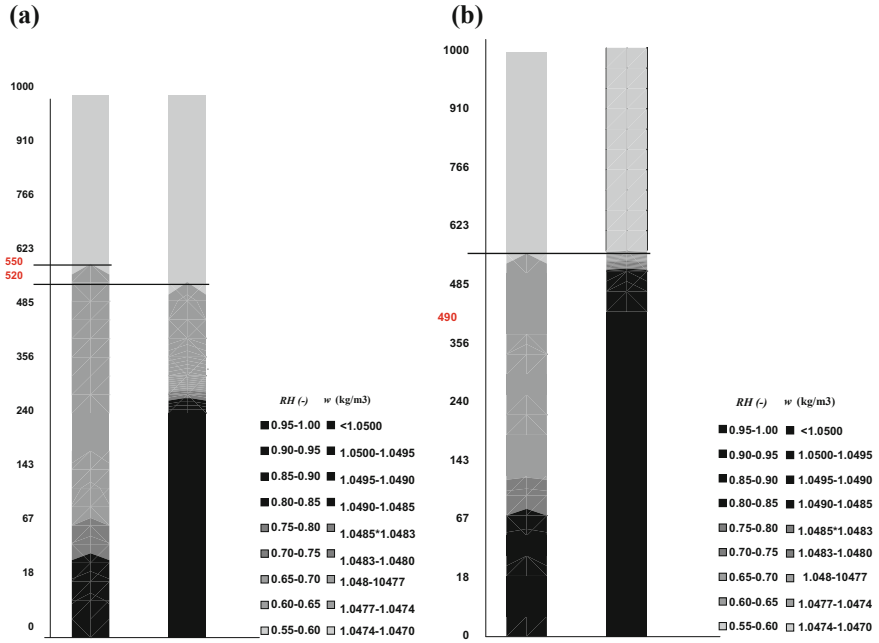

Fig. 7.10 Variation of rising damp front with relative humidity and water content for (**a**) Configuration 1 and (**b**) Configuration 3

surfaces. Figure 7.10a, b show the variation of rising damp front with relative humidity and water content for different boundary conditions. These figures also show that the numerical results are in accordance with the experimental and analytical values obtained (see Table 7.3).

The research group is currently studying whether these values may have adverse consequences in terms of the long-term deterioration of the wall materials [99]. As we understand how salts dissolve in water and their behaviour in terms of crystallization/dissolution, the target, in future, will be to scale the new rising damp treatment system to avoid crystallization/dissolution problems.

7.2.4.2 In-Field

The hygro-regulable system was installed in a church in Northern Portugal (see Fig. 7.11a). Inside the building, two hygro-regulable mechanical ventilation subsystems were installed (see Fig. 7.11b). In the Southside subsystem, air was admitted through grids located inside the building, and was extracted into the cloister. Extraction was controlled by a hygro-regulable engine of variable speed [26]. The system had two probes for measuring relative humidity and

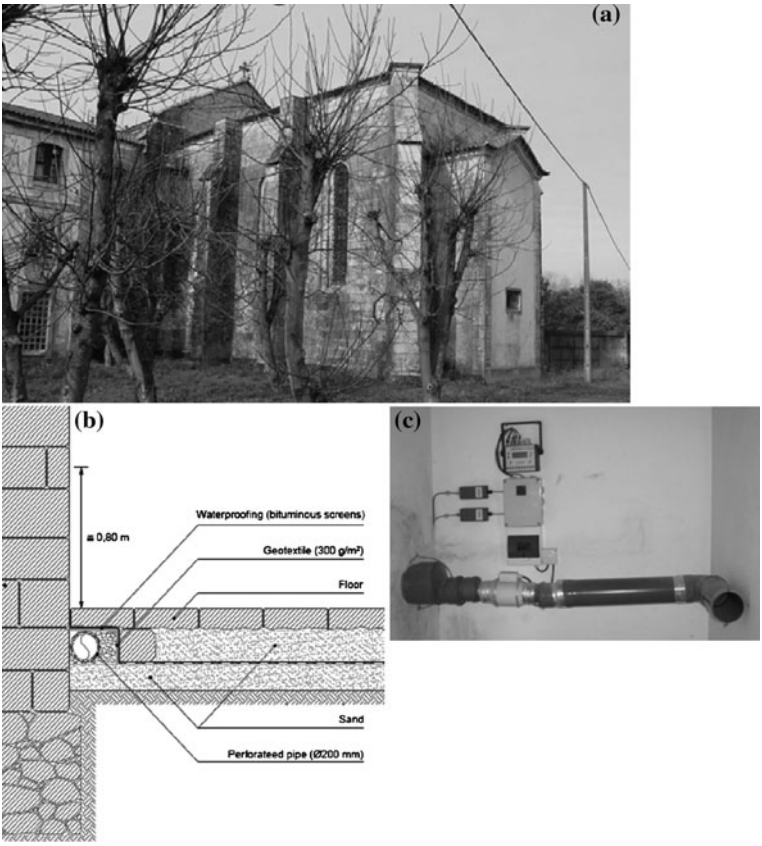

Fig. 7.11 (**a**) Church in Northern Portugal; (**b**) Wall base ventilation system and (**c**) Data acquisition and recording system

temperature, two transmitters, a control module and a data acquisition system for recording results (see Fig. 7.11c).

The system installed in the church initially began operating whenever the relative humidity at the exit was 5% higher than the relative humidity at the entrance. The idea was to admit dry air comparing to the air inside the system. This criterion was found to be inadequate, as it meant that the system was operating at periods when condensation occurred inside it. Consequently, a new criterion was proposed with a view to optimizing the system, based upon the difference in vapour pressure (ΔP) at the exit and entrance. The system now began functioning whenever the ΔP was positive.

Figure 7.12a, b shows the functioning periods of the ventilator, in a north and south wall, and the importance of HUMIVENT device in rising damp treatment, by the quantity of water vapour extracted during the five months analyzed (272.3 kg in the north wall and 170.2 kg in the south wall).

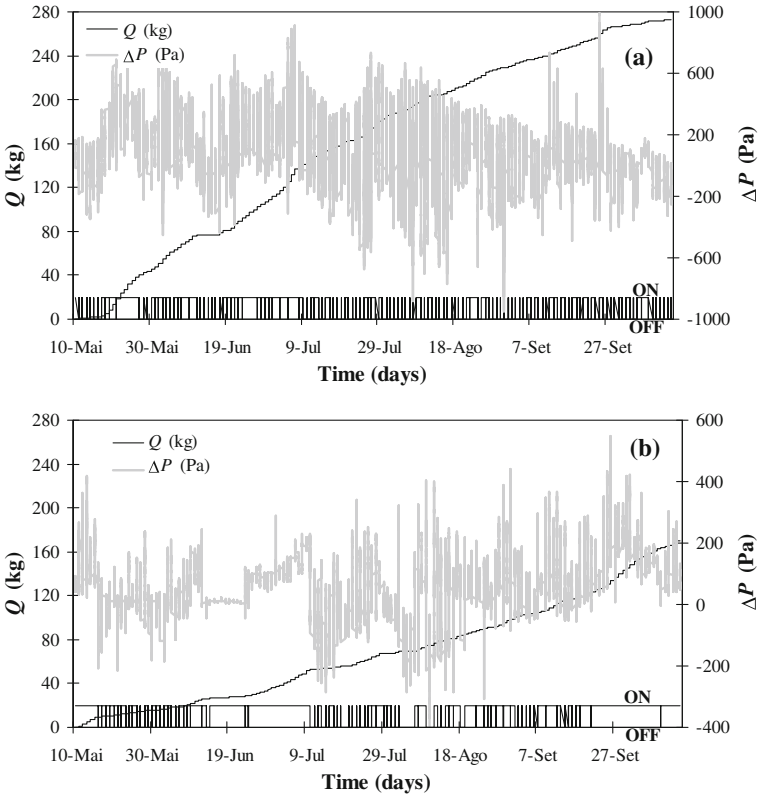

Fig. 7.12 Quantity of water vapour extracted, pressure differential and functioning of system: (**a**) North wall and (**b**) South wall

The entry of air with very low relative humidity could generate the crystallization of salts existing in the building materials, threatening its durability. For this reason, the relative humidity value at the entrance had to be limited. The relative humidity scores recorded, which range from 60 to 95%, are not considered to present a risk of salt crystallization/dissolution inside the system, consider the salts detected in those area. However, the problem might arise in another type of external climate or with other salts type [99]. In that case the HUMIVENT device must also limit the inlet relative humidity value.

In conclusion, the mechanisms of moisture transfer are complex, particularly in terms of rising damp in historic buildings. As rising damp is one of the main causes of decay in these buildings, it is important to study the factors related to this phenomenon.

The traditional techniques currently used to minimise rising damp are not effective or too expensive, in particular when dealing with walls of considerable thickness and heterogeneous materials. Laboratory tests on 20 cm thick limestone walls show that an efficient way of treating rising damp in historic buildings is to ventilate the wall base using the HUMIVENT device.

The analytical model of rising damp predicts steady height of rise figures that are consistent with laboratory observations, which provide a good validation of the analysis. Using this model it is possible to scale the HUMIVENT system, optimise it and predict its behaviour. The numerical simulation results are similar to those obtained experimentally and analytically, which provide a qualitative validation of the results obtained.

7.3 Bubbles and Drops in Porous Structures

Transport of mixtures is encountered in many industrial processes and engineering applications. More specifically, one of the most interesting cases is that of a discontinuous phase (droplets) situated within a flowing continuous aqueous phase. A typical example of this may be found in the oil industry, and is related to unconventional behavior found in some heavy oil reservoirs where a disconnected gas phase (gas bubbles) inside a connected liquid phase (heavy oil) is observed over periods of time long enough to consider that such a phase distribution governs flow dynamics [29, 42]. Qualitatively speaking, the aspects of such a transport process are rather well understood. In general, droplets are transferred by convection and diffusion while their population is strictly governed by local hydrodynamic phenomena [85]. It is very difficult to obtain a globally valid description for the consequent transient (dynamic) behavior of the microstructure of such a mixture due to the high geometrical complexity of such a configuration. For example, the domain size could grow because the domains may coalesce under flow conditions and a break-up process sets in when they are large enough to be affected.

Renewed interest in this field originates from theoretical investigations on the flow in porous materials using conventional computations [30, 73, 89], the Lattice Boltzmann Method [46, 68, 69] and pore network simulators [13, 24]. These approaches focus mainly on flow dynamics for multiphase and multi-component fluids rather than the microstructure formation where limited research has been done [59, 60, 64, 70, 98].

The exemplar application presented here aims to describe this micro-structure especially for mixtures flowing in a homogeneous porous medium under laminar conditions. In particular, the scope of this theoretical study is to investigate the physical/geometrical parameters and the flow conditions which could assure the mixture's homogeneity (water/droplets, i.e. continuous/discontinuous phase) in terms of mean droplet size. Focus is on the domain sizes formed during this process and the approach taken here is the so-called '$S\gamma$ concept', i.e. the 'moments of distribution', for droplet size description [52], where an arbitrary number of moments of the domain size distribution is used to describe the microstructure. In the same study, the method was also described in relation to experiments on bubble coalescence. Subsequently, Klahn et al. [57] and Agterof et al. [3] used the same method to analyze experiments on the transient behavior of emulsion droplet break-up in an impeller flow, and to analyze the behavior of double emulsions. All these examples demonstrated the method's power, and will be explained in detail below.

In this section the $S\gamma$ method is extended to phenomena related to porous structures. The problem examined here is the laminar flow of a biphasic mixture in a homogeneous porous medium. The domain size for the two phases not only depends on the flow itself but also on the break-up and coalescence processes taking place because of the flow. The method's fundamental idea is that the evolution of the moments of a distribution can be analyzed using a transport equation including a convective term, which can be coupled to the local flow characteristics, which should not be affected by the presence of droplets. This assumption is valid only for droplet sizes small enough to follow the bulk flow and adequately assure the homogeneity of the flowing mixture (see Eq. 7.38) and relative discussion). The source terms in the transport equation describe the local phenomena (break-up and coalescence) that affect particle size distribution. The main advantage of this approach is that analytical expressions (including probability parameters) could be derived for the characteristic magnitudes, leading to successful simulations through common and rather simple CFD techniques.

7.3.1 Moments of Distribution ($S\gamma$)

The domain (droplet) size distribution can be described by a collection of moments of the distribution as [3, 52, 57]:

$$S_\gamma = n \int_0^\infty d^\gamma P(d)\,\mathrm{d}d \tag{7.32}$$

where γ is an integer indicating the specific moment, n is the total number density, and $P(d)$ is the droplet size distribution. Some of these moments can be related directly to physical properties of the dispersion. More precisely [3, 52]:

$$S_0 = n \int_0^\infty P(d)\,\mathrm{d}d = n \tag{7.33}$$

is the total number of droplets (number density),

$$S_2 = n \int_0^\infty d^2 P(d)\,\mathrm{d}d \tag{7.34}$$

is the specific interfacial area, and

$$S_3 = n \int_0^\infty d^3 P(d)\,\mathrm{d}d = \frac{6\varphi}{\pi} \tag{7.35}$$

is an expression of the volume fraction, φ.

It can be easily shown that for two different γ values, the corresponding $S\gamma$ functions can produce a useful characteristic diameter $d_{\gamma_1\gamma_2}$ according to the relation:

$$d_{\gamma_1\gamma_2} = \left(\frac{\int_0^\infty d^{\gamma_1} P(d)\,\mathrm{d}d}{\int_0^\infty d^{\gamma_2} P(d)\,\mathrm{d}d}\right)^{\frac{1}{\gamma_1-\gamma_2}} = \left(\frac{S_{\gamma_1}}{S_{\gamma_2}}\right)^{\frac{1}{\gamma_1-\gamma_2}} \quad \text{for } \gamma_1 \neq \gamma_2 \tag{7.36}$$

From geometrical and physical point of view, the most interesting $d_{\gamma_1\gamma_2}$ is the area-weighted mean droplet diameter, d_{32}, given as:

$$d_{32} = \frac{S_3}{S_2} = \frac{\int_0^\infty d[d^2 P(d)]\,\mathrm{d}d}{\int_0^\infty d^2 P(d)\,\mathrm{d}d} \tag{7.37}$$

It is worth noticing that this diameter is a spatially averaged size which here is considered to represent the actual droplet size.

The main advantage of the $S\gamma$ function is that it satisfies the transport equation [52]. Starting from the well-known population balance equation and following the mathematical route presented by Kamp et al. [52], the following transport equation can be derived:

$$\frac{\partial nP(d)}{\partial t} + \nabla \cdot (\underline{u} nP(d)) = G - E \tag{7.38}$$

where $\underline{u}$ is the local velocity vector and G, E are the generation and the extinction terms, respectively. These terms are strongly related to droplet creation (break-up) and death (coalescence).

After multiplying each term by d^γ and subsequently integrating over all particle sizes, the following equation can be obtained:

$$\frac{\partial}{\partial t}\left[\int_0^\infty d^\gamma nP(d)dd\right] + \nabla \cdot \left[n\int_0^\infty d^\gamma \underline{u} P(d)dd\right] = \int_0^\infty (G-E)d^\gamma\,dd \tag{7.39}$$

By reversing the order of differentiation and integration, Eq. 7.39 can also be written as a transport equation:

$$\frac{\partial S_\gamma}{\partial t} + \nabla \cdot (\underline{u}_\gamma S_\gamma) = h_i^{(\gamma)} \tag{7.40}$$

where:

$$\underline{u}_\gamma = \frac{\int_0^\infty P(d)\underline{u}(d)d^\gamma dd}{\int_0^\infty P(d)d^\gamma dd} \tag{7.41}$$

Expression (7.41) equals the local velocity vector, $\underline{u}$, if the droplets have the same velocity as the flowing continuous bulk phase, an assumption adopted here. It is assumed that the local flow field is independent of the droplets, thus their mean

diameter is too small to affect the homogeneity of the flowing phase. Even for porosities close to unity, the mean droplet size must be lower than 10^{-6} m for creeping or laminar flow conditions [64] to satisfy the above assumption.

In Eq. 7.40, $h_i^{(\gamma)}$ is the source term related to droplet break-up and coalescence, expressed in terms of the moments of the distribution. For the majority of engineering applications, transport equation (7.41) can be simplified to:

$$\frac{\partial S_\gamma}{\partial t} + \underline{u} \cdot \nabla S_\gamma = h_i^{(\gamma)} \tag{7.42}$$

When the flow problem is uncoupled from the transport one, the velocity field $\underline{u}$ can be obtained from typical CFD flow simulations.

7.3.2 Determination of Source Terms

Since the governing phenomena in the fluid phase are the droplet break-up and coalescence processes, the source term of the previous equation can be expressed as:

$$h_i^{(\gamma)} = h_{br}^{(\gamma)} + h_{cl}^{(\gamma)} \tag{7.43}$$

where $h_{br}^{(\gamma)}$ and $h_{cl}^{(\gamma)}$ are the respective source terms that can be modeled explicitly.

Break-up occurs when droplet diameter becomes larger than a critical value, d_{cr}. This value is related to the critical capillary number as follows:

$$d_{cr} = \frac{2\,\sigma\, Ca_{cr}}{\eta_c\,\dot{\gamma}} \tag{7.44}$$

where Ca_{cr} is the critical capillary number, $\dot{\gamma}$ is the local velocity gradient, η_c is the viscosity of the continuous phase, and σ is the interfacial tension. This critical diameter also depends on viscosity ratio and flow type, as discussed by Grace [32] and Stone [90].

The break-up source term, in its generic form, can be written as [49]:

$$h_{br}^{(\gamma)} = \int_0^\infty K_{br}(d)\Delta S_\gamma^{br}(d) n P(d) dd \tag{7.45}$$

where K_{br} is the break-up rate, and $\Delta S_\gamma^{br}(d)$ is the change in $S\gamma$ due to a single break-up event in a droplet of size d. An expression for $\Delta S_\gamma^{br}(d)$ follows from the conservation of dispersed phase volume when droplet-fragments are formed [101]:

$$\Delta S_\gamma^{br}(d) = d^\gamma \left(N_f (d)^{\frac{3-\gamma}{3}} - 1 \right) \tag{7.46}$$

where N_f is the number of fragments formed. Since the break-up rate K_{br} is conversely analogous to the break-up time τ_{br}, the break-up source term becomes:

$$h_{br}^{(\gamma)} = \int_0^{\infty} \left[\frac{d^{\gamma}}{\tau_{br}(d)} \left(N_f \, (d)^{\frac{3-\gamma}{3}} - 1 \right) \right] n \, P(d) \, \mathrm{d}d \quad \text{for} \;\; d > d_{cr} \tag{7.47}$$

Coalescence depends not only on collisions but also on coalescence probability, thus the generic form of the coalescence source term is [15]:

$$h_{cl}^{(\gamma)} = \int_0^{\infty} \int_0^{\infty} K_{cl}(d, d') \Delta S_{\gamma}^{cl}(d, d') n^2 P(d) P(d') \mathrm{d}d \mathrm{d}d' \tag{7.48}$$

where K_{cl} is the collision rate, whose detailed description follows. The change in $S\gamma$ due to a single coalescence event, $\Delta S_{\gamma}^{cl}(d, d')$, between two droplets of diameters d and d', respectively, can be expressed as [15]:

$$\Delta S_{\gamma}^{cl}(d, d') = d^{\gamma} \left[\left(1 + \left(\frac{d'}{d} \right)^3 \right)^{\gamma/3} - \left(1 + \left(\frac{d'}{d} \right)^{\gamma} \right) \right] \tag{7.49}$$

or, by involving a uniform distribution with an equivalent mean diameter d_{eq}:

$$\Delta S_{\gamma}^{cl} = d_{eq}^{\gamma} (2^{\gamma/3} - 2) \tag{7.50}$$

Consequently, the coalescence source term becomes [3]:

$$h_{cl}^{(\gamma)} = (2^{\gamma/3} - 2) \left(\frac{6 \, \varphi}{\pi} \right)^2 K_{cl}(d_{eq}) \, d_{eq}^{\gamma - 6} \tag{7.51}$$

The coalescence rate $K_{cl}(d_{eq})$ is typically given as [15]:

$$K_{cl}(d_{eq}) = K_{coll}(d_{eq}) \, P_{coal}(d_{eq}) \tag{7.52}$$

where $P_{coal}(d_{eq})$ is the coalescence probability of a single collision event, which is a function of the equivalent diameter, d_{eq}, and $K_{coll}(d_{eq})$ is analogous to the product $k_{coll} \; u_{rel}(d_{eq})$, representing the Smoluchowski collision rate [3].

Finally, the coalescence source term is given as:

$$h_{cl}^{(\gamma)} = (2^{\gamma/3} - 2) \left(\frac{6 \, \varphi}{\pi} \right)^2 k_{coll} \; u_{rel}(d_{eq}) \; P_{coal}(d_{eq}) \; d_{eq}^{\gamma - 4} \tag{7.53}$$

7.3.3 Simulations

Our research team conducted a series of simulation experiments during last 15 years to study the above theoretical approach at laboratory scale. The simulations were carried out using a FORTRAN code especially developed for this

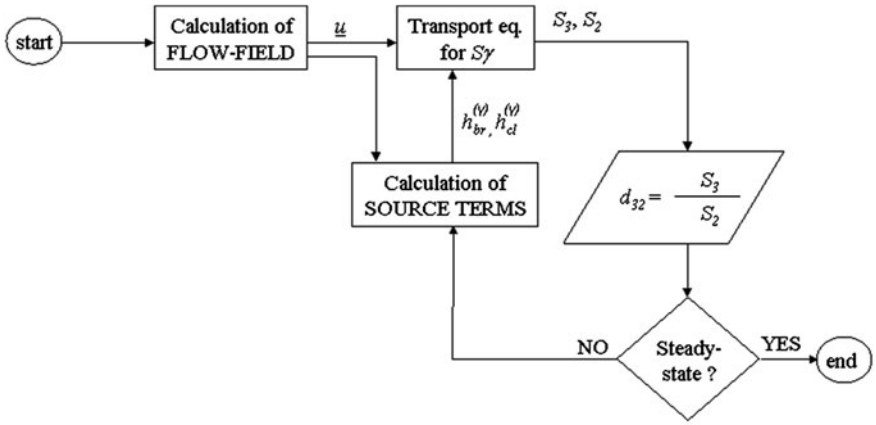

Fig. 7.13 Flowchart of the simulation algorithm

work. Calculations were performed on a simple PC equipped with an Intel© Duo Core processor and 2 GB of RAM, using Windows XP© operating system. On average, the calculations took about 12 h.

To adequately simulate the above problem, the algorithmic procedure shown in Fig. 7.13 was used. The procedure followed was: firstly the characteristics of the flow in a porous medium were calculated using standard CFD methods, and subsequently the local velocity field obtained was used in a transport equation to analyze the evolution of the domain size distribution. Although the algorithm aims at a steady-state solution, the intermediate results before reaching steady-state conditions could be used to study transient behavior of the mean droplets, by taking into account only the steady-state flow field. For the numerical solution of the transport boundary value problems, a non-uniform finite differences scheme with up winding was used for discretization in space, with the resulting linear systems of equations solved again using SOR.

To define a realistic domain for the solution of the flow and transport problem, a porous medium was constructed in the form of a spherical particle assemblage. Specifically, representation of the biphasic domains considered was achieved by the random deposition of spheres of a given radius in a box of specified dimensions as presented in Fig. 7.14, depicting a sample medium of $\varepsilon = 0.72$. The structure was digitized and the phase function was determined to obtain the specified porosity. The size of the digitized domains was $102 \times 102 \times 102$ and the length of the simulation box was approximately ten times the sphere radius.

To obtain the velocity field it is necessary to solve the Stokes equations:

$$\nabla p = \mu \nabla^2 \underline{u} \tag{7.54}$$

$$\nabla \cdot \underline{u} = 0 \tag{7.55}$$

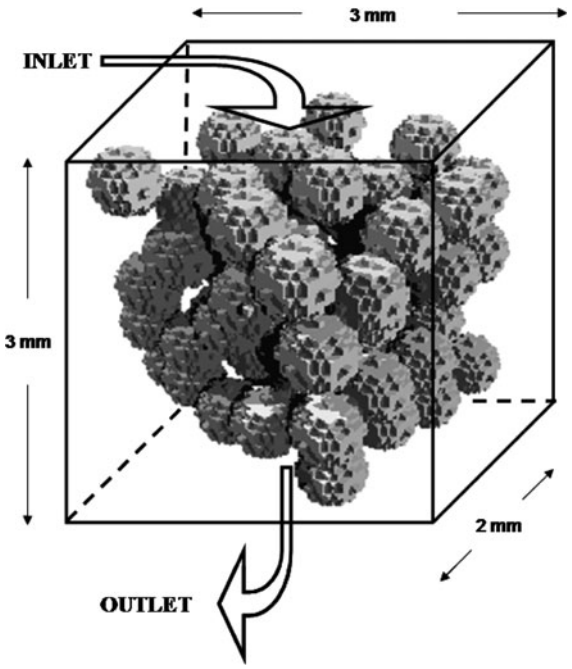

Fig. 7.14 Stochastically constructed 3-D porous medium. (Sample medium of $\varepsilon = 0.72$)

where $\underline{u}$, p, and μ are the velocity vector, pressure field and fluid viscosity, respectively. The procedure for solving the three dimensional Stokes flow problem is rather complicated in the vicinity of a porous structure [51, 54]. In the present study, a staggered marker-and-cell (MAC) mesh was involved, the pressure was defined at the cell center, and the velocity components were defined along the corresponding face boundaries. The resulting linear system of equations was solved by a successive over-relaxation (SOR) method. An initial estimate of p was determined by solving a Laplace equation. Next, the velocity vector $\underline{u}$ was calculated from the corresponding momentum balance and the continuity equation $\nabla \cdot \underline{u} = 0$. The pressure was corrected using an artificial compressibility equation of the form:

$$\frac{dp}{dt} = \beta \nabla \cdot \underline{u} \tag{7.56}$$

Essentially, the method adds an artificial density time derivative that is related to the pressure by an artificial equation of state $p = \beta\rho$, where β is an artificial compressibility factor. Similar to the compressible momentum equation, $c = \beta^{1/2}$ is an artificial speed of sound and for stability reasons during the iterative procedure, its magnitude should be such that the respective artificial Mach number, $M = \frac{R}{c} \max_D \left(\sum_i u_i^2 \right)^{1/2}$ is low ($M \ll 1$), where R is the relevant Reynolds number. In the limiting case of $R \to 0$, which is the present case, any finite value

of β should meet this criterion. Thus, $\beta = 1$ was chosen here, although it has been evident that the exact value cannot have any effect on the final (steady state) results since at steady state the artificial density time derivative is zero. The above steps were repeated until convergence was reached. This numerical scheme to determine the velocity field has been widely validated in terms of both the velocity field and the corresponding permeability [2, 20].

Regarding boundary conditions, one of the six surfaces of the simulated domain was considered an inlet, while the opposite surface was assigned as an outlet. The other four domain surfaces were assumed to be spatially periodic, both in geometrical and physical (flow and transport) terms.

The differential equations for the flow-field were integrated with the following initial and boundary conditions:

$$\underline{u}(\underline{r},\, t = 0) = 0 \tag{7.57}$$

$$P(\underline{r},\, t = 0) = P_0 \tag{7.58}$$

$$u(\underline{r} = \text{void space of the inlet},\, t) = u_{in} \tag{7.59}$$

$$\nabla \cdot \underline{u}(\underline{r} = \text{void space of the inlet},\, t) = 0 \tag{7.60}$$

$$P(\underline{r} = \text{void space of the inlet},\, t) = P_{in} \tag{7.61}$$

$$P(\underline{r} = \text{void space of the outlet},\, t) = P_0 \tag{7.62}$$

$$\underline{u}(\underline{r} = \text{void/solid interfaces},\, t) = 0 \tag{7.63}$$

Initial conditions (7.57) and (7.58) indicate a quiescent mixture in the void space of the porous medium, while boundary conditions (7.59–7.61) impose a uniform (plug) flow at the inlet. Obviously, non-zero values appear only on the surfaces of the void space, since velocity and pressure equal zero at the solid phase. Boundary condition (7.62) imposes the necessary pressure gradient for the Stokes flow, while Eq. 7.63 expresses the non-slip condition at the fluid/solid interfaces throughout the porous medium.

The transport equation (7.42) was integrated with the following initial and boundary conditions:

$$S_\gamma(\underline{r},\, t = 0) = 10^{-16} \tag{7.64}$$

$$S_\gamma(\underline{r} = \text{void space of the inlet},\, t) = (S_\gamma)_{in} \tag{7.65}$$

$$\nabla \cdot S_\gamma\,(\underline{r} = \text{void space of the inlet},\, t) = 0 \tag{7.66}$$

$$S_\gamma(\underline{r} = \text{void space of the outlet},\, t) = (S_\gamma)_{out} \tag{7.67}$$

$$\nabla \cdot S_\gamma\,(\underline{r} = \text{void/solid interfaces},\, t) = 0 \tag{7.68}$$

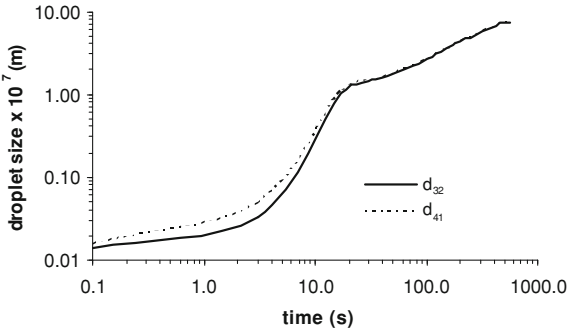

Fig. 7.15 Evolution of the average droplet size for two different sets of $S\gamma$ values

The initial condition (7.64) indicates a very low initial droplet population, while boundary conditions (7.65–7.67) impose a gradient for the $S\gamma$. Equation 7.68 expresses neutral behavior at the fluid/solid interfaces, while spatial periodicity is again assumed for the domain's other outer surfaces. Note that the above conditions are independent of the γ values.

7.3.4 Algorithm Validation and Findings

To examine the validity of the solution scheme, the algorithm was tested against its consistency. More precisely, different sets of $S\gamma$ values should lead to similar distribution parameters, i.e. to the same mean droplet size, by using Eq. 7.36. Such a test was performed by carrying out simulations for two specific sets of $S\gamma$ values, namely S_1, S_2, S_3 and S_4. These distributions lead to mean droplet size through $d_{32} = \dfrac{S_3}{S_2}$ and $d_{41} = \left(\dfrac{S_4}{S_1}\right)^{\frac{1}{3}}$, which should theoretically be the same. The mesh and time step size were the same in both cases.

Figure 7.15 depicts this comparison and the two curves represent the evolution of d_{32} and d_{41} through time. Since the results are very similar, this plot proves the self-consistency of $S\gamma$ modeling.

Since droplet size is represented by d_{32}, the solution scheme is hereafter used only for $\gamma = 2$ and $\gamma = 3$, thus the relevant source terms become:

$$h_{br}^{(2)} = \int_0^{\infty} \left[\frac{d^2}{\tau_{br}(d)} \left(\sqrt[3]{N_f(d)} - 1 \right) \right] n\, P(d)\, \mathrm{d}d \tag{7.69}$$

$$h_{cl}^{(2)} = -0.740079 \left(\frac{6\,\varphi}{\pi} \right)^2 k_{coll}\; u_{rel}\,(d_{eq})\; P_{coal}\,(d_{eq})\, d_{eq} \tag{7.70}$$

$$h_{br}^{(3)} = 0 \tag{7.71}$$

$$h_{cl}^{(3)} = 0 \tag{7.72}$$

Table 7.4 Parameters used in the simulations

Parameter	Units	Expression/value	Reference/comment
$N_f(d)$	(–)	$2.69 f_1(\lambda)\left(\frac{d}{d_{cr}}\right)^3$	[32]
$\tau_{br}(d)$	(s)	$\frac{2\eta_c\, d}{\sigma} f_2(\lambda)$	[32]
$f_1(\lambda), f_2(\lambda)$	(–)	• 1 for the current case • Other values/expressions for the specific case studied	
d_{cr}	(m)	Eq. 7.44	Calculated at each point and time step
σ	(N m^{-1})	0.0728	Since the current work is purely theoretical, the continuous phase is supposed to be water
Ca_{cr}	(–)	1	[72]
η_c	(centipoises)	0.89	Since the current work is purely theoretical, the continuous phase is supposed to be water
$P(d)$	(–)	$\frac{1}{d\,\hat{\sigma}\sqrt{2\pi}} \exp\left(-\frac{\left(\ln d - \ln \overline{d}\right)^2}{2\,\hat{\sigma}^2}\right)$	[52]
$\hat{\sigma}$	(–)	0.1	[15, 52]
$\overline{d}$	(m)	3 x 10^{-8}	[15, 52]
$k_{coll}\, u_{rel}\,(d_{eq})$	(m s^{-1})	$0.6667\underline{u}$	[15, 52]
$P_{coal}(d_{eq})$	(–)	Follows the log-normal distribution accordingly to the droplets' diameters	[15, 52]
d_{eq}	(m)	$\left(\frac{6\varphi}{\pi S_\gamma}\right)^{\frac{1}{3-\gamma}}$	[3]
φ	(–)	$\frac{4}{3}\pi(d_{32})^3 \frac{1}{0.03\times0.03\times0.02} n$	Calculated at each time step
n	(m^{-3})	whole algorithm and Eq. 7.33	Calculated once from the solution for S_0

For the results presented here, the simulation's parameters are presented in Table 7.4.

The time evolution of the average characteristic droplet size, d_{32}, is presented in Fig. 7.16 up to the critical time where the system reaches the steady-state situation. The maximum size is observed at $t = 550$ s, mainly due to competition between the hydrodynamic phenomena, i.e. break-up and coalescence. At $t = 900$ s, the droplet size distribution levels off taking a rather constant value for longer time scales.

This dynamic behavior of the system is clarified in Fig. 7.17 which shows the relative significance of the source terms. The individual source terms have been normalized by their maximum value, i.e. $h_{br}^{(\gamma)} = h_{br}^{(\gamma)} / MAX\left\{h_{br}^{(\gamma)}\right\}$, $h_{cl}^{(\gamma)} = h_{cl}^{(\gamma)} / MAX\left\{h_{cl}^{(\gamma)}\right\}$, to fit the same graph. However, their initial values are non-zero because the model assumes

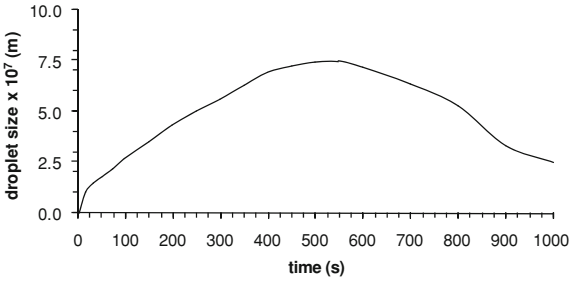

Fig. 7.16 Characteristic average droplet size (d_{32})

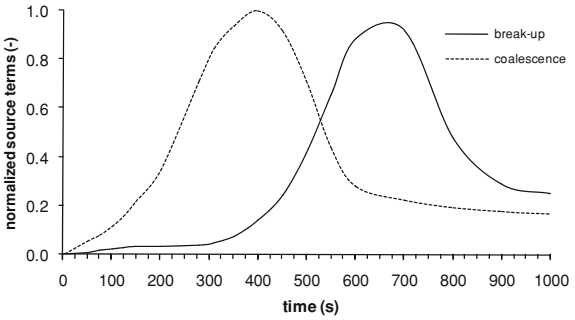

Fig. 7.17 Relative significance of source terms

that droplet size evolution also initiates from a non-zero value (see Fig. 7.16). As shown in Fig. 7.17 during the first 550 s, coalescence dominates over break-up as the particles are quite small, therefore, droplet size increases. At $t = 550$ s the contributions of break-up and coalescence are balanced, thus particle size reaches a peak. After 550 s, break-up becomes more significant than coalescence, thus particle size decreases until $t = 900$ s. It is worth noting that the time period considered in the simulation is critical for result validity. Obviously, the simulation time is strongly dependent on the specific medium's geometry and the flow characteristics. The simulation time for the above presented results was t = 1,000 s for the given porosity ($\varepsilon = 0.72$) and velocity field ($u = 1$ m/s). A more detailed study of the influence of these parameters follows.

Although porosity has not been directly included in the specified transport equations, it is a crucial parameter for the microstructure transport phenomena since it affects significantly the local flow field and mass transport regime through the void space in the porous medium. The effect of porosity is presented in Figs. 7.18 and 7.19. The time instant when droplet diameter reaches the maximum value, t_{max}, is presented in Fig. 7.18 as a function of the medium's porosity. It is notable that t_{max} varies little with porosity, and this is because droplet size is much smaller than mean pore diameter, leaving therefore the droplets unaffected by the presence of the solid phase, even for the lowest porosity value. Furthermore, lower porosity values correspond to higher coalescence probabilities because the lower

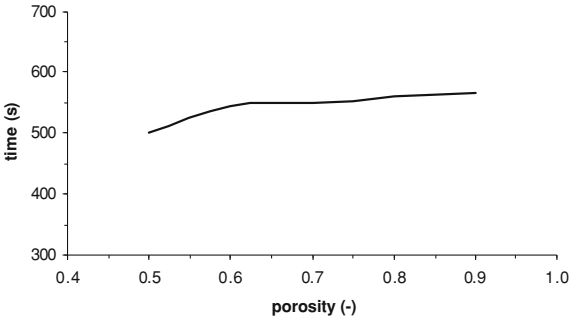

Fig. 7.18 Effect of porosity on the time when MAX{d_{32}} is observed

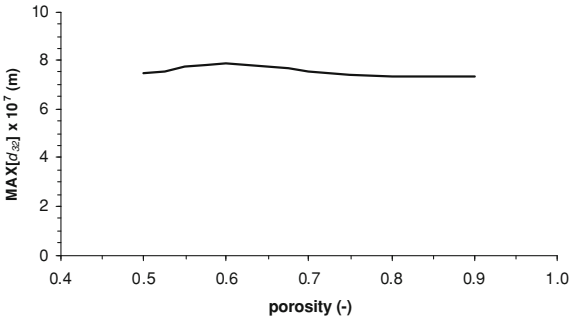

Fig. 7.19 MAX{d_{32}} as a function of porosity

the porosity, the narrower the path for a bubble to escape without any collision and, therefore, the higher the coalescence source term. In addition, break-up is not affected significantly by porosity, because $h_{br}^{(\gamma)}$ is non-zero only for diameters larger than a critical diameter value, whose order of magnitude is 10^{-7} m which corresponds to porosity values of order of magnitude 10^{-5} for feasible characteristic lengths. Actual porosity values range from 0.5 to 0.9, assuring that $h_{br}^{(\gamma)}$ is not practically affected by the porosity. Therefore, the only influence on decreasing porosity is the enhancement of $h_{br}^{(\gamma)}$ which corresponds to earlier times for maximum diameters with lower porosity. However, this influence on t_{max} does not correspond to any significant change in the absolute value of maximum diameter, as shown in Fig. 7.19. Indeed, maximum values of source terms remain rather unaffected by porosity, leading to a fairly constant maximum diameter, despite the fact that the time when these maximum values occur varies with porosity, as discussed previously.

Finally, Figs. 7.20 and 7.21 show the effect of flow intensity on droplet size. As depicted in Fig. 7.20, an increase in inlet velocity value corresponds to delayed appearances of maximum diameters. Indeed, as velocity increases i.e. convection dominates diffusion, it is easier for droplets to collide, therefore, the coalescence source term increases. Furthermore, a very low increment of the break-up source term is also expected because the higher the velocity, the easier for a droplet to

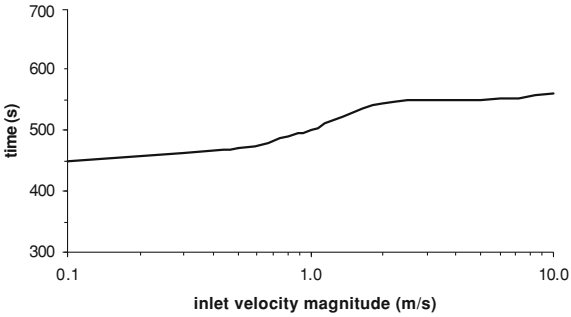

Fig. 7.20 Effect of inlet velocity magnitude on the time when MAX{d_{32}} is observed

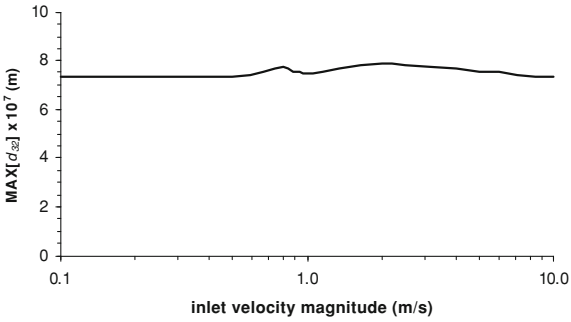

Fig. 7.21 MAX{d_{32}} as a function of inlet velocity magnitude

reach and interfere with the solid phase. As the phenomenon dominantly influenced by the flow is coalescence, maximum diameter is observed later for higher convective regimes. Again, and for the same reasons as those discussed above, this does not seem to affect significantly the maximum diameter (see Fig. 7.21).

7.4 Fluid Flows Through Porous Media in Fuel Cells

During the last decades, gradually increasing global energy demands, rising environmental and health concerns, and depletion of natural resources, have intensified the need to discover new energy production technologies. These new technologies should utilize current fuels more effectively by raising the efficiency of the energy production units, and be more environmentally friendly by reducing CO_2 emissions. Fuel cells seem to be one potential answer to this goal and offer energy policy makers energy independence under fully environmentally friendly conditions.

Fuel cells are electrochemical devices that directly convert chemical energy from gaseous fuels into electricity by overcoming Carnot limitations. Theoretically, they can reach high efficiencies and, unlike batteries, are able to provide a continuous supply of electric power when replenished with fuel. Furthermore, fuel cells are very compact units without moving parts, therefore ensuring silent operation, fewer material design constraints and reasonable portability.

Of the fuel cells available, SOFCs present considerable advantages due to their high operating temperature. These high temperatures favor electrochemical reaction kinetics permitting the use of low cost metal catalysts and they promise higher efficiencies when recovering the high energy waste heat (electrical efficiencies of 45–50% can be achieved). Furthermore, SOFC operation allows external or even internal reforming reactions to occur, thus fuels such as carbon monoxide and hydrocarbons considered poisonous to low temperature fuel cells, can be used with minimal fuel processing [1, 33, 48, 55, 76]. Despite these benefits, they do present some drawbacks regarding the materials used caused mainly by the high temperatures, such as thermal expansion of the different fuel cell components and stability issues due to mechanical deficiencies and catalyst deactivation. However, much effort has been given to fabricating new, cost effective materials with improved physical and electrochemical characteristics that would enhance both SOFC performance and stability [95].

Due to the variety of their advantages, SOFCs are considered ideal candidates for various applications. As mentioned previously, they operate at high temperatures and the waste thermal energy (waste heat) produced can be recovered in combined heat and power systems (CHP) to produce electricity and power in large-scale distributed power generation systems as well as in small-scale domestic heat and power production units, taking full advantage of the fuel used. SOFCs are also considered to be useful as auxiliary power units (APUs) for various electrical systems in cooking and transportation, such as in vehicle air conditioning and portable electronics, i.e. cell phones and personal computers. In addition, SOFCs can be used for the chemical cogeneration of electricity and chemical compounds with the use of appropriate materials. They could also be an alternative choice for remote distributed power generation either in areas with no grid supply, such as isolated islands, or when local power production is necessary, such as small power units [19, 63, 67, 84].

According to their temperature operation, SOFCs can be classified into low-, intermediate- and high-temperature types with operating temperatures between 773–823 K, 823–1,073 K and 1,073–1,273 K, respectively. Regarding geometrical aspects and design, one of the most commonly used geometries is the tubular one, initially introduced by Siemens-Westinghouse [86]. The operation principal here is that the tubular fuel cell comprises a unique tube, the air is supplied internally, and the fuel is thought to flow in the surroundings. Another design is the planar geometry in which the PEN assembly is surrounded by the collectors [43, 74]. According to the flow direction of air and fuel, planar geometry SOFCs can be subdivided into (1) co-flow planar SOFCs, where air and fuel flow in the same direction, (2) counter-flow, where they flow in opposite directions, and (3) cross-flow, where they flow perpendicular to each other [25]. Tubular and planar geometries can be both electrolyte or electrode (anode or cathode) supported [4, 92].

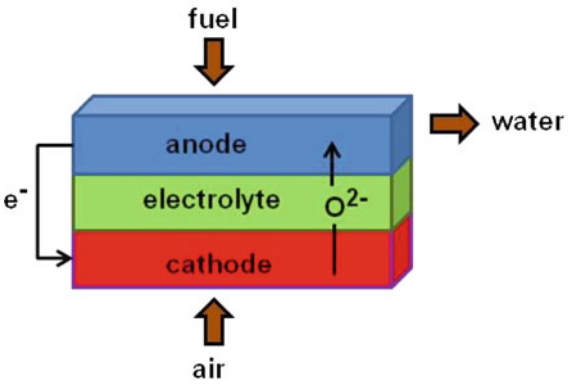

Fig. 7.22 A typical SOFC configuration

7.4.1 Solid Oxide Fuel Cell Configuration

A typical SOFC consists of an anode and a cathode compartment between which a catalyst (electrolyte) layer exists. Air flow enters one gas channel and the other channel is continuously supplied by a feeding mixture (usually a hydrogen-rich mixture containing some higher hydrocarbons with carbon monoxide and dioxide). The electrolyte has high ionic and minimum electronic conductivity and it prevents fuel crossover and mixing of the gas supplies. The fuel is electrochemically oxidized by the oxygen ions, O^{2-}, formed at the cathode electrode by the oxygen reduction reaction. These ions migrate through the electrolyte to the anode. It is evident that the same number of electrons must be transferred through the electrolyte in order to preserve equilibrium between the electrodes. The electrons released at the anode compartment flow via an external electrical circuit. In most cases, the principle operation of a typical fuel cell incorporates the formation of water from hydrogen and oxygen, and the production of electricity and heat. A typical configuration of an SOFC is presented in Fig. 7.22.

7.4.2 Electrochemical and Surface Reactions

The most significant advantage of SOFCs compared to other fuel cell types, is that they allow wide fuel flexibility due to high operational temperature and the materials used. As a result, apart from hydrogen (H_2), SOFCs can be fed with carbon monoxide (CO) and synthesis gas (H_2 and CO of various ratios), as well as natural gas and hydrocarbon fuels (coal fuels). The electrochemical reactions take place at the interface between the catalyst, the ionic conductor, and the gas phase–the so-called three-phase boundary layer (TPB). The electrochemical oxidation reactions of H_2 and CO occurring at the anode electrode can be described by:

$$H_2 + O^{2-} \rightarrow H_2O + 2e^- \tag{7.73}$$

$$CO + O^{2-} \rightarrow CO_2 + 2e^- \tag{7.74}$$

Experiments have shown that the electrochemical oxidation rate of H_2 is significantly higher (1–2.5 times) than that of CO [18, 71, 91], thus a large number of existing models neglect the contribution of CO in the production of current density.

With the use of appropriate anode cermets, such as Cu-YSZ and Ni-YSZ, direct oxidation of hydrocarbons and/or alcohols is possible in SOFCs [47, 77, 107]. In general, assuming that the fuel can be expressed as $C_nH_mO_p$ where $p = 0$ or $p = 1$ denoting hydrocarbon or alcohol fuels, respectively, the electrochemical oxidation reactions can be expressed as:

$$C_nH_m + (2n + 0.5m)O^{2-} \rightarrow nCO_2 + 0.5mH_2O + (4n + m)e^-, \text{ where } p = 0 \tag{7.75}$$

$$C_nH_mO + (2n + 0.5m - 1)O^{2-} \rightarrow nCO_2 + 0.5mH_2O + (4n + m - 2)e^-, \text{ where } p = 1 \tag{7.76}$$

Atmospheric air (humidified or not) and, rarely, pure O_2 is often introduced into the cathode gas channel. At the cathode electrode, the electrochemical oxygen reduction taking place can be written as:

$$0.5O_2 + 2e^- \rightarrow O^{2-} \tag{7.77}$$

and in case of $C_nH_mO_p$ fuels the reaction is:

$$(n + 0.25m)O_2 + (4n + m)e^- \rightarrow (2n + 0.5m)O^{2-}, \text{ where } p = 0 \tag{7.78}$$

$$(n + 0.25m - 0.5)O_2 + (4n + m - 2)e^- \rightarrow (2n + 0.5m - 1)O^{2-}, \text{ where } p = 1 \tag{7.79}$$

Apart from the electrochemical reactions, in practice, numerous homogeneous or heterogeneous chemical reactions may appear in an SOFC. The most common reactions included in simulation models are presented below. In general, the water gas shift reaction (WGS):

$$CO + H_2O \leftrightarrow CO_2 + H_2 \tag{7.80}$$

is applied when both hydrogen and carbon monoxide are present, and is usually assumed to be in equilibrium.

To effectively use hydrocarbon fuels they should be partially reformed to H_2 and CO by the internal or external steam reforming reactions as follows [1]:

$$C_nH_m + nH_2O \rightarrow nCO + (0.5m + n)H_2, \text{ where } p = 0 \tag{7.81}$$

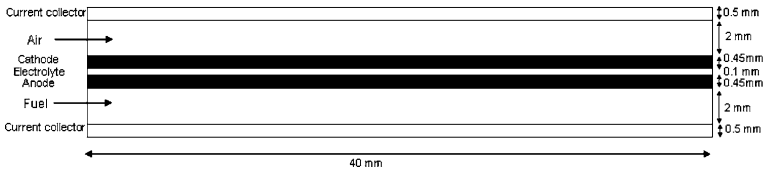

Fig. 7.23 Simulated SOFC geometry

$$C_nH_mO + (n-1)H_2O \rightarrow nCO + (0.5m + n - 1)H_2, \text{ where } p = 0 \tag{7.82}$$

Additionally, the presence of hydrocarbons may lead to carbon formation. To study the adverse effects of carbon on catalyst deactivation, the Boudouard reaction [7, 41, 66, 96, 104]

$$2CO \leftrightarrow C + CO_2 \tag{7.83}$$

and cracking reactions (where applicable)

$$C_nH_m \leftrightarrow nC + 0.5mH_2 \tag{7.84}$$

may be introduced.

7.4.3 Transport Phenomena in Gas Channels

The fundamental transport phenomena occurring in gas channels are flow and heat transfer, mass transport and charge transfer. These are described by the equations of continuity, momentum and species (neutral or charged) conservation equation. Therefore, the velocity field, temperature profile, gas composition and electric potential distribution of the fuel cell can be calculated. For better insight on the processes occurring, fuel cell geometry can be divided into two general regions. The first is the non-porous region, which refers to the gas channels, and the second includes all the porous parts of the fuel cell i.e. anode and cathode electrode, the dense electrolyte and even the current collectors. A two-dimensional cut of the fuel cell is depicted in Fig. 7.23, where the dimensions have been chosen in accordance with Ramakrishna et al. [83].

Firstly, for non-porous regions the mass conservation equation (continuity equation) can be written as:

$$\frac{\partial \rho}{\partial t} + \nabla \cdot (\rho \underline{U}) = 0 \tag{7.85}$$

where $\underline{U}$ is the velocity vector, ρ is the fluid density, and t is time.

Velocity in fuel cell gas channels is usually quite low, so the assumption of laminar flow can be considered accurate. As a result, for compressible fluids and neglecting gravitational effects, the momentum equation is:

$$\frac{\partial}{\partial t}(\rho \underline{U}) + \nabla \cdot (\rho \underline{U}\,\underline{U}) = -\nabla P + \nabla \cdot \overline{\tau} \tag{7.86}$$

where P is the pressure, and $\overline{\tau}$ is the shear stress tensor.

By neglecting radiation, the energy conservation equation becomes:

$$\frac{\partial}{\partial t}(\rho h) + \nabla \cdot (\rho \underline{U} h) = \nabla \cdot (k \nabla T) + \frac{\partial P}{\partial t} + \dot{Q} \tag{7.87}$$

where h is the total enthalpy of the fluid, k is the thermal conductivity of the mixture, and $\dot{Q}$ describes the additional thermal sources due to exothermic/endothermic reactions. The mass fraction of each gas species can be computed by the species conservation equation as follows:

$$\frac{\partial}{\partial t}(\rho Y_i) + \nabla \cdot (\rho \underline{U} Y_i) = \nabla \cdot \underline{J_i} + \dot{\omega}_i \tag{7.88}$$

where Y_i are the mass fractions of the ith chemical species, $\dot{\omega}$ is the production/destruction rate of the $i-$th chemical species in gas phase due to homogeneous reactions, and $\underline{J_i}$ is the species i mass diffusion flux.

Several approaches are used in the literature to calculate the mass diffusion flux, but this is beyond the scope of this analysis. The simplest model used to calculate the species diffusion flux is Fick's law:

$$\underline{J_i} = \rho D_i \nabla Y_i \tag{7.89}$$

where D_i is the mass diffusion coefficient of species i in the mixture.

Although several models for the estimation of diffusivity have been presented in the literature, in the present study the mass diffusion coefficient for gas channels is obtained through the Schmidt number, Sc, according to the relation:

$$D_i = \frac{\mu}{Sc} \tag{7.90}$$

where μ is the viscosity of the gas species.

The above differential equations are all strongly coupled and should be integrated along with the appropriate boundary conditions, which are application dependant.

7.4.4 Transport Phenomena in Porous Media

Porous materials are widely used in SOFC applications and particularly at the anode and cathode electrodes, since they present large catalytic surface areas. All the transport phenomena described above should be modified slightly to incorporate the porous nature of the electrodes and simulate the transport processes since porous material structure implies mass transport limitations.

Analytically, the mass conservation equation in a porous medium can be written as:

$$\frac{\partial}{\partial t}(\varepsilon\rho) + \nabla \cdot (\varepsilon\rho\underline{U}) = 0 \tag{7.91}$$

where ε is the porosity of the medium representing the volume occupied by the pores to the total volume of the porous media.

In porous regions, the momentum conservation equation becomes:

$$\frac{\partial}{\partial t}(\varepsilon\rho\underline{U}) + \nabla \cdot (\varepsilon\rho\underline{UU}) = -\varepsilon\nabla P + \nabla \cdot (\varepsilon\bar{\tau}) + \frac{\varepsilon^2\mu}{\kappa}\underline{U} \tag{7.92}$$

where μ is the viscosity of the fluid, and κ is the permeability representing the square of the volume to surface area ratio of the porous material. Note that the last term of Eq. 7.92 represents Darcy's law and describes the superficial velocity in the porous medium [23].

The energy conservation equation inside a porous medium, written in terms of enthalpy, takes into account thermal convection and conduction, species diffusion contributions, and chemical reaction (neutral or electrochemical) effects on temperature. It can be written as:

$$\frac{\partial}{\partial t}(\varepsilon\rho h) + \nabla \cdot (\varepsilon\rho\underline{U}h) = \nabla \cdot \left(k_{eff}\nabla T + \sum_{i=1}^{Ng}\underline{J}_i h_i\right) + \varepsilon\bar{\tau}\nabla\underline{U} + \varepsilon\frac{dP}{dt} - j_i\eta + \frac{|\underline{i}|^2}{\sigma} \tag{7.93}$$

where k_{eff} is the effective thermal conductivity of the mixture, N_g is the total number of gas species in the system, and h_i is the enthalpy of the ith species. The temperature gradient is significantly affected inside the porous material by the electrochemical reactions and consequently both Joule heating and electrical work affect energy transfer. This effect is described by the last two terms of the energy transfer equation.

By taking into account the combination of porous and solid parts of the porous medium, the effective thermal conductivity of this medium can be defined as [35]:

$$k_{eff} = -2k_S + \frac{1}{\frac{\varepsilon}{2k_S + k_F} + \frac{1-\varepsilon}{3k_S}} \tag{7.94}$$

where k_F is the thermal conductivity of fluid parts of the porous medium, and k_S is the thermal conductivity of solid parts of the porous medium.

The conservation equation of the $i-th$ gas species is given by the relation:

$$\frac{\partial}{\partial t}(\varepsilon\rho Y_i) + \nabla \cdot (\varepsilon\rho\underline{U}Y_i) = \nabla \cdot \underline{J_i} + \dot{\omega}_i \tag{7.95}$$

where Fick's model can also be applied, given as:

$$\underline{J_i} = \rho D_{i,eff} \nabla Y_i \tag{7.96}$$

where $D_{i,eff}$ is the effective mass diffusion coefficient of species i.

To consider the porosity, ε, and tortuosity, τ, of the porous medium, a number of correlations can be found in the literature such as the Daggan model. However, the most applicable is the Bruggeman correlation, defined as [79]:

$$D_{i,eff} = \varepsilon^{\tau} D_i \tag{7.97}$$

To calculate species diffusion fluxes, apart from Fick's model applied here, several other models cam be used such as the Stefan-Maxwell model for multi component systems, and the Dusty Gas model (DGM), which incorporates both the Stefan-Maxwell formulation and the Knudsen diffusion [11, 94].

Regarding charge conservation in conducting materials, the sum of all current flows should be zero based on electro-neutrality. Thus, the current conservation equation is:

$$\nabla \cdot \underline{i} = 0 \tag{7.98}$$

where $\underline{i}$ is the current density vector

However, based on Newman and Tabias [75], charge transport consists of electronic and ionic phase transports. During electrochemical reactions electrons are either transferred from the pores (ionic phase) to the solid region (electronic phase) or vice versa, i.e. electron transfer is expressed as the transfer current, j_T, where:

$$-\nabla \cdot \underline{i_F} = \nabla \cdot \underline{i_S} = j_T \tag{7.99}$$

where $\underline{i_F}$ is the current density vector flowing through the pores (ionic phase), and $\underline{i_S}$ is the current density vector flowing through the solid parts of the porous medium (electronic phase). By applying Ohm's law, the transfer current yields:

$$\nabla \cdot (\sigma_F \nabla \varphi_F) = -\nabla \cdot (\sigma_S \nabla \varphi_S) = j_T \tag{7.100}$$

where σ_F and σ_S are the ionic phase conductivity and the solid phase conductivity, respectively, and φ_F and φ_S are the ionic potential of the fluid and the electric potential of the solid, respectively.

For the non-conducting electrolyte Eq. 7.100 becomes:

$$\nabla \cdot (\sigma_F \nabla \varphi_F) + \nabla \cdot (\sigma_S \nabla \varphi_S) = 0 \tag{7.101}$$

and the current transfer j_T can be defined through the Butler-Volmer equation as:

$$j_T = \frac{j_0 \left(\frac{A}{V}\right)}{\prod_{i=1}^{N} \left[C_{i,ref}\right]^{a_{i_e}}} \left[\exp\left(\frac{a_a F}{RT}\eta\right) - \exp\left(-\frac{a_c F}{RT}\eta\right)\right] \prod_{i=1}^{N} [C_i]^{a_{i_e}} \tag{7.102}$$

where $i.e$ indexes the electrochemical reactions, j_0 is the exchange current density, a_a and a_c are the anodic and cathodic charge transfer coefficients as determined by the Tafel plots respectively, N is the total number of reacting species, $[C_i]$ is the near wall molar concentration of the ith reacting species or expressed in mass fractions as $[C_i] = \rho \frac{Y_i}{M_i}$, where M_i is the molar weight of the $i - th$ species, $[C_{i,ref}]$ is the molar concentration at a reference state at the inlet, and a_k is the concentration exponent. The overpotential, η, can be expressed as the potential difference between the solid phase and the porous phase potential:

$$\eta = \varphi_S - \varphi_F \tag{7.103}$$

In surface reactions occurring at porous/catalyst interfaces, the volumetric reaction rate (production/destruction of a gas species i) can be computed assuming a balance between the reaction flux and the diffusion flux on the surface [50]. This rate is given as:

$$\dot{\omega} = \rho D_i \frac{Y_i - Y_{P,i}}{\delta} \left[\frac{A}{V}\right]_{eff} \tag{7.104}$$

where $Y_{P,i}$ is the mass fraction of the ith species in the pore fluid, $[A/V]_{eff}$ denotes the effective surface to volume ratio of the catalyst and represents the catalyst load, and δ is the diffusion length scale. For electrochemical reactions, the production/destruction rate is expressed through the current transfer by the relation:

$$\dot{\omega} = (b_{PR} - b_R)\frac{j_T}{F} \tag{7.105}$$

where b_{PR} and b_R are the stoichiometric coefficients of the products and reactants, respectively.

7.4.5 Simulations

Planar SOFC geometry was used for the three-dimensional approach. This geometry consists of seven separated volumes: the fuel and air channel where the corresponding mixtures are introduced, the porous anode and cathode electrodes where the reactions occur, the dense electrolyte through which oxygen ions migrate to reach the anode electrode, and finally the anode and cathode contacts. In the present study, both H_2 and CO were assumed to react with oxygen ions, in accordance with Eqs. 7.73 and 7.74. Regarding the Butler-Volmer equation (Eq. 7.102), the exchange current density was set to $j_0 = 10^{11}\text{Am}^{-3}$ for the anode and $j_0 = 10^{10}\text{Am}^{-3}$ for the cathode, where the charge transfer coefficients for both electrodes were $a_a = 0.7$ and $a_c = 0.7$. The electrochemical reactions were assumed to occur only in the porous electrodes and precisely on the three-phase boundary layer. It was also assumed that no other reactions occurred either on

the porous interface or in the bulk phase. The feeding stream was assumed to be a reformate mixture of 9.6% H_2, 26.0% CO, 2.16% CO_2 and 42.8% H_2O on w.t.% basis, and typical atmospheric air composition was applied at the cathode channel (23.3% O_2 and 76.7% N_2 on w.t. basis).

Regarding the boundary conditions, the mass flow rates for the anodic and cathodic mixtures were assumed to be constant and equal to 3.0×10^{-7} kg/s and 4.0×10^{-6} kg/s, respectively, while pressure of 1 atm was set at the inlets and outlets. Considering no accumulation, zero mass flux was set at the walls and outlets. Additionally, preheated mixtures of 1,173 K entered the fuel cell, while zero heat flux was set at all the other boundaries. Finally, the constant value of zero overpotential was set to the anode contact, while the overpotential of the cathode contact was set to -0.7 V.

Both electrodes were modeled as isotropic porous media and their physical characteristics are as follows [58, 83]: porosity was $\varepsilon = 0.4$ for the anode, $\varepsilon = 0.01$ for the electrolyte, and $\varepsilon = 0.5$ for the cathode; permeability was $\kappa = 10^{-12}$ $m^2$for the anode and cathode, and $\kappa = 10^{-18}$ m^2 for the electrolyte; solid phase electrical conductivity was $\sigma_S = 10,000\ \Omega m^{-1}$ for the anode, $\sigma_S = 10^{-20}\,\Omega m^{-1}$ for the electrolyte, and $\sigma_S = 7,700\,\Omega m^{-1}$ for the cathode; ionic phase electrical conductivity was $\sigma_F = 10\,\Omega m^{-1}$ for both the electrodes and the electrolyte.

To calculate the density, ρ, it was assumed that the gases followed the ideal gas law, and the kinetic theory of gases was used to estimate viscosity, μ. Specific heat, c_p, was derived by fittings to experimental JANNAF curves, and mass diffusivity was calculated by imposing 0.7 to the Schmidt number.

To achieve residual values less than 10^{-4} for all the quantities and assuming steady state conditions, the numerical solution of the transport problems was obtained by the commercial package CFD-ACE$^+$ by ESI-Group©, which is based on the finite volume method, together with all the appropriate boundary conditions. The three-dimensional fuel cell was discretized in space using a structured grid of 33, 516 cells.

7.4.6 Results and Discussion

The typical distributions for the main physical quantities (velocity, temperature mass fractions and overpotential) obtained for constant gas inlet mixture and temperature for both fuel and air mixtures are presented in Figs. 7.24, 7.25, 7.26, 7.27, 7.28, 7.29. These are contour plots in a two-dimensional cut in the middle plane of the fuel cell. Figure 7.24 shows the developed velocity profile, which was parabolic for both flow channels, satisfying the non-slip conditions applied on the walls. Due to the mass flow rates imposed, high velocity values can be seen in the air channel and lower velocity values in the fuel channel, while zero velocities are observed in the porous media. The highest value observed was approximately 5 m/s, which can be considered quite high, but necessary to satisfy the energy demands of the system in terms of cooling, and maintain active chemical reactions.

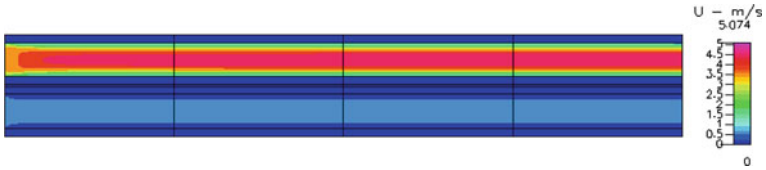

Fig. 7.24 Velocity profile

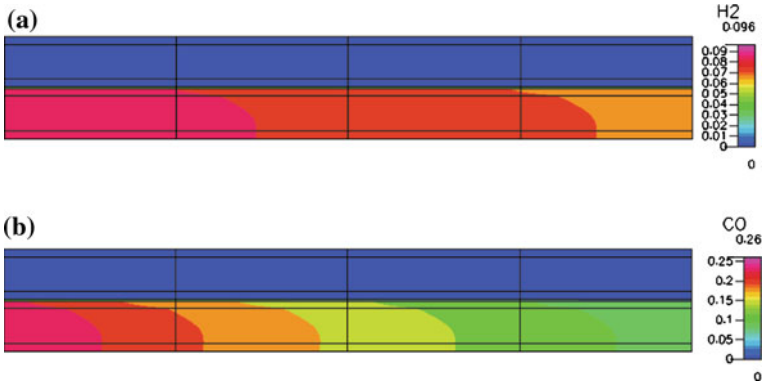

Fig. 7.25 Mass fraction profiles for (**a**) hydrogen and (**b**) carbon monoxide

The molar fractions of the major reactants and products along the fuel cell are presented in Figs. 7.25, 7.26. Figure 7.25 shows that hydrogen and carbon monoxide are consumed at the anode channel and anode electrode. Furthermore, their fractions decrease with distance, due to the electrochemical reaction controlling the system. The consumption of both species is accompanied by relative production of both CO_2 and H_2O, in accordance with the relative reaction rates.

A small depletion of oxygen can be observed at the cathode and the cathode channel (Fig. 7.27). This can be attributed to its participation in the electrochemical reactions. The O_2 gradient is fairly small since the air mass flow rate is high enough to avoid oxygen depletion that would lower fuel cell performance, while the highly convective regime does not favor the electrochemical reactions.

Temperature varies along the fuel cell length from 1,173 K imposed at the inlet boundary to 1,256 K at the outlet (Fig. 7.28). This temperature variation is strongly affected by the electrochemical reactions occurring at the anode electrode. Hydrogen and carbon monoxide electro oxidation reaction is exothermic, thus a certain amount of heat is released in the cell and transferred locally due to convection and conduction. Consequently, temperature increase can be observed along the length of the cell and it is evident that convectional effects prevail at the air channel due to the developing velocities. Finally, the over potential profile is depicted in Fig. 7.29. The over potential at the anode electrode is higher compared to that at the cathode electrode due to fuel depletion at the anode channel. It should

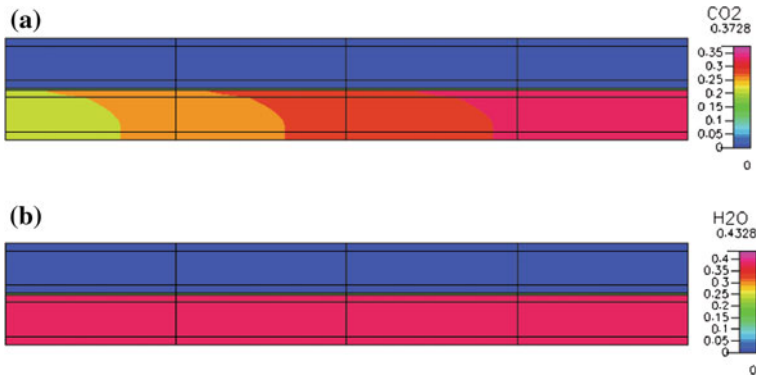

Fig. 7.26 Mass fraction profiles for (**a**) carbon dioxide and (**b**) steam

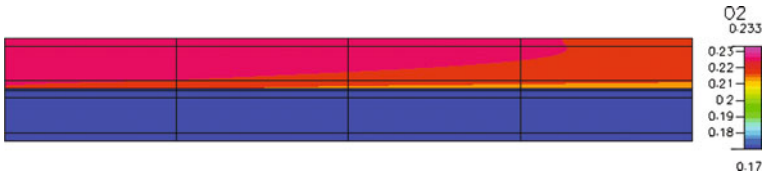

Fig. 7.27 Mass fraction profile for oxygen

also be mentioned that over potential increases along the anode electrode and this rise is followed by the reduction of active species mass fractions i.e. H_2 and CO.

7.5 Multi Phase Transport in Porous Media

Numerous physicochemical processes exist where an aqueous phase coexists and/or interacts with a non-aqueous liquid phase in a porous medium. Many of these processes have significant importance in terms of industrial and technological applications, e.g. tracer transport in petroleum reservoirs, chemical contamination of soils and aquifers, long-term interaction between liquefied or chilled foods with packaging materials. The description of such processes often relies on mathematical models as experimentation can be expensive or difficult.

In the presence of porous media, the need for a realistic description of the structure of a porous medium significantly increases the mathematical complexity of a model. However, elements of the microstructure must be captured when moving from the pore level to the macroscopic level, where process performance must often be studied. A number of techniques for up scaling from the pore-scale to the macroscopic scale in porous media have been developed. Of specific interest here is volume-averaging [14, 78, 105, 106], which is very useful when pore scales

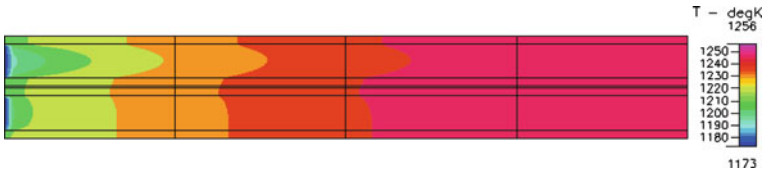

Fig. 7.28 Spatial distribution for temperature

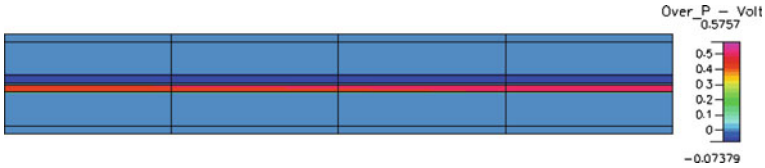

Fig. 7.29 Overpotential profile

and macroscopic scales are separated. Starting from the relevant differential equations at the pore level and using the spatial averaging theorem, after several mathematical manipulations based on scale separation [102, 103], one is lead to unit-cell problems to estimate macroscopic quantities [80, 81]. Spatial averaging techniques allow the integral effect of the influence of pore geometry on transport to be captured in the mathematical formulation.

Typically, macroscopic models involve an exchange term to describe the rate of mass transfer between the two phases. The majority of existing theoretical works derived such models based on the assumption of the mass exchange equilibrium between the aqueous and non-aqueous liquid phases [27, 28, 45, 62]. This assumption of infinitely fast diffusion in the non-aqueous phase, simplifies mathematical modeling and consequent simulations [37, 82, 88]. It is necessary to determine the validity of this assumption. When the assumption is relaxed, the resulting unit-cell problem includes mass transport between the two phases (the "aqueous" and the "non-aqueous" liquids), thus accounting for inter-phase diffusion and partitioning. Its solution provides expressions required for the macroscopic mass-transfer coefficient. Various model pore geometries are used to obtain representative results. An ab initio calculation is also presented, in which the Stokes equations are solved in typical pore geometries and compared with the volume-averaging results.

7.5.1 Theoretical Background

Consider a multi-phase domain consisting of a flowing aqueous phase (β-phase), an immobile non-aqueous liquid phase (γ-phase) and a solid phase (σ-phase), as schematically depicted in Fig. 7.30.

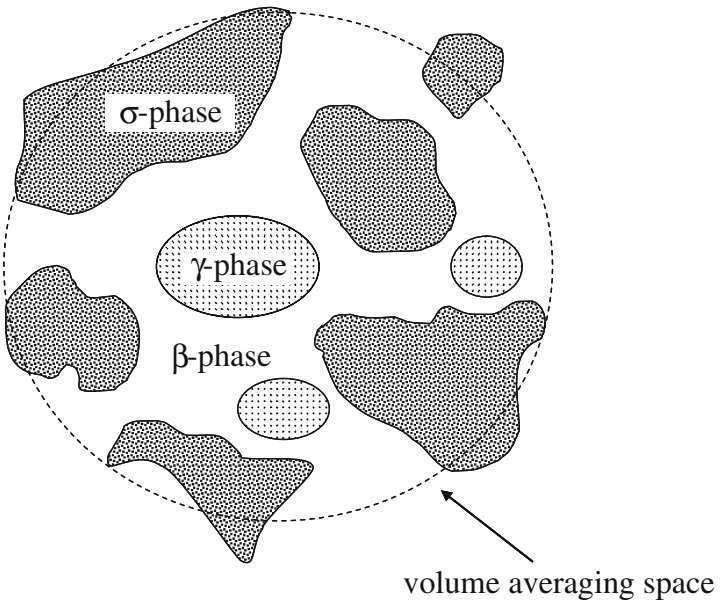

Fig. 7.30 Schematic depiction of a typical representative volume

The assumption of a motionless γ-phase is a good approximation for several applications, such as water or gas tracer transport in hydrocarbon reservoirs where the oil phase rests practically immobile (e.g. residual saturation), slow dissolution of NonAqueous Phase Liquids (NAPLs) in underground porous formations, and packing porous pellets with a wetting fluid. To relax this assumption, one should backtrack to techniques (e.g. Lattice-Boltzmann) capable of solving the flow problem while simultaneously determining the dynamic distribution of fluid phases in the considered porous domain. This approach, however, requires significant computational resources [10]. A partitioning tracer is advected by the flowing β-phase and partitioned in the immobile phase into which it is diffusing. It is assumed that the solid phase is physicochemically neutral, i.e. the tracer is neither adsorbed nor reacts with the σ-phase. The governing processes in the β-phase are diffusion and advection, and diffusion in the γ-phase. The mass exchange at the $\beta\gamma$ interface is characterized by the diffusion and partitioning properties of the tracer. The macroscopic modeling of the processes is typically described by the following advection–dispersion-reaction equations:

$$\varepsilon_\beta \frac{\partial \langle C_\beta \rangle}{\partial t} + \langle \mathbf{v} \rangle \cdot \nabla \langle C_\beta \rangle = \varepsilon_\beta D_\beta^* \nabla^2 \langle C_\beta \rangle - \alpha \left(\langle C_\beta \rangle - \frac{1}{K} \langle C_\gamma \rangle \right) \tag{7.106}$$

$$\varepsilon_\gamma \frac{\partial \langle C_\gamma \rangle}{\partial t} = \varepsilon_\gamma D_\gamma^* \nabla^2 \langle C_\gamma \rangle + \alpha \left(\langle C_\beta \rangle - \frac{1}{K} \langle C_\gamma \rangle \right) \tag{7.107}$$

where ε_β, ε_γ denote the volume fraction of the β- and γ-phase, respectively, v is the velocity vector in the β-phase, D^*_β, D^*_γ are the macroscopic dispersion coefficients in the β- and γ- phase, respectively, and K is the partitioning coefficient. Brackets denote spatial averages.

The knowledge of several parameters (e.g., of the mass-transfer coefficient and the dispersion tensor) is required to solve the above macroscopic equations. As previously noted, volume averaging can provide these expressions when scale separation exists. The main theoretical work in this field is that of Quintard and Whitaker [82], which presents methods for the calculation of the mass-transfer coefficient and the dispersion tensor under the assumption of infinitely fast diffusion in the γ-phase. This corresponds to an almost constant concentration profile in the γ-phase and permits decoupling of the mass transport problems in the two phases. Mass exchange between the two phases has been also modeled by various researchers, considering either a controlling diffusive process macroscopically described by first order kinetics, or an advection process [5, 9, 22, 38, 65, 96]. What is proposed here is a more rigorous extension that considers non-equilibrium partitioning of the tracer and mass transfer in both phases. Three-dimensional model pore geometries were considered in the following numerical illustrations, where the immobile γ-phase may be distributed as either wetting films or non-wetting aggregates (blobs). The objective is to estimate the mass transport coefficient and investigate the effect of different structural and physicochemical parameters under non-equilibrium partitioning. Otherwise, the volume averaging approach is conventional and consists of the algorithm presented in Sect. 5.5.

7.5.2 Formulation of the Problem

The pore-level transport of the tracer in the β-phase is described by the diffusion–advection equation

$$\frac{\partial C_\beta}{\partial t} + \nabla \cdot (vC_\beta) = D_\beta \nabla^2 C_\beta \tag{7.108}$$

where C_β is concentration, t is time, v is the fluid velocity, and D_β is the diffusivity in the β-phase. Since the γ-phase is assumed to be immobile, the diffusion equation describes the transport of the tracer in that phase:

$$\frac{\partial C_\gamma}{\partial t} = D_\gamma \nabla^2 C_\gamma \tag{7.109}$$

where C_γ and D_γ are concentration and diffusivity in the γ-phase, respectively. Zero-flux boundary conditions apply to the solid–liquid interfaces:

$$\mathbf{n}_{\beta\sigma} \cdot \nabla C_\beta = 0 \quad \text{at} \quad A_{\beta\sigma} \tag{7.110}$$

$$\mathbf{n}_{\gamma\sigma} \cdot \nabla C_\gamma = 0 \quad \text{at} \quad A_{\gamma\sigma} \tag{7.111}$$

as the transported species do not absorb or react at the solid. At interface $A_{\beta\gamma}$ between trapped and flowing phases, the following conditions apply:

$$C_\gamma = KC_\beta \tag{7.112}$$

$$D_\beta \mathbf{n}_{\beta\gamma} \cdot \nabla C_\beta = D_\gamma \mathbf{n}_{\beta\gamma} \cdot \nabla C_\gamma \tag{7.113}$$

where K is the partitioning coefficient. Equation 7.112 describes the partition equilibrium, while (7.113) expresses the flux continuity at the interface. This mass exchange description is more general than in previous works [82] and does not assume fast diffusion in the γ-phase as used by Quintard and Whitaker [82], De Smedt and Wierenga [88] and Gvirtzam et al. [37].

Following the volume averaging procedure [82], local concentrations and velocities are next decomposed into interstitial averages and fluctuations:

$$C_\beta = \langle C_\beta \rangle^\beta + C'_\beta \tag{7.114}$$

$$C_\gamma = \langle C_\gamma \rangle^\gamma + C'_\gamma \tag{7.115}$$

$$\mathbf{v}_\beta = \langle \mathbf{v}_\beta \rangle^\beta + \mathbf{v}'_\beta \tag{7.116}$$

which are subsequently substituted into the governing differential equations. Invoking separation of scales to discard small terms, linearizing and following Quintard and Whitaker [82], the representation below can be easily obtained when assuming an isotropic medium of uniform porosity and constant volume fractions:

$$C'_\beta = \mathbf{b}_\beta \cdot \nabla \langle C_\beta \rangle^\beta + s_\beta \left(\frac{1}{K} \langle C_\gamma \rangle^\gamma - \langle C_\beta \rangle^\beta \right) \tag{7.117}$$

$$C'_\gamma = \mathbf{b}_\gamma \cdot \nabla \langle C_\gamma \rangle^\gamma + s_\gamma \left(\frac{1}{K} \langle C_\gamma \rangle^\gamma - \langle C_\beta \rangle^\beta \right) \tag{7.118}$$

where b_β, b_γ, s_β and s_γ are closure variables satisfying specific boundary value problems.

7.5.3 The Closure Problems

It can be readily shown that variable s_β of the β-phase satisfies the boundary value problem [82]:

$$\mathbf{v}_\beta \cdot \nabla s_\beta = D_\beta \nabla^2 s_\beta - \varepsilon_\beta^{-1} \alpha \tag{7.119}$$

with boundary conditions:

$$s_\beta = 1 + \frac{s_\gamma}{K} \text{ at } A_{\beta\gamma} \tag{7.120}$$

$$D_\beta \mathbf{n}_{\beta\gamma} \cdot \nabla \mathrm{s}_\beta = D_\gamma \mathbf{n}_{\beta\gamma} \cdot \nabla \mathrm{s}_\gamma \text{ at } A_{\beta\gamma} \tag{7.121}$$

$$\mathbf{n}_{\beta\sigma} \cdot \nabla s_\beta = 0 \text{ at } A_{\beta\sigma} \tag{7.122}$$

and the compatibility condition:

$$\langle s_\beta \rangle = 0 \tag{7.123}$$

Similarly, variable s_γ of the γ-phase satisfies the following problem:

$$D_\gamma \nabla^2 s_\gamma = -\varepsilon_\gamma^{-1} \alpha \tag{7.124}$$

$$\mathbf{n}_{\gamma\sigma} \cdot \nabla s_\gamma = 0 \text{ at } \quad A_{\gamma\sigma} \tag{7.125}$$

$$\langle s_\gamma \rangle = 0 \tag{7.126}$$

where the mass transfer coefficient, α, is given by:

$$\alpha = \frac{D_\beta}{V} \int\limits_{A_{\beta\gamma}} \mathbf{n}_{\beta\gamma} \cdot \nabla s_\beta dA \tag{7.127}$$

The above equation can be simplified by introducing the transformation $s_\beta = 1 + \alpha\psi_{\beta s}$ and $s_\gamma = \alpha\psi_{\gamma s}$, and in dimensionless form:

$$s_\beta = 1 + \alpha^* \zeta_\beta \tag{7.128}$$

$$s_\gamma = \alpha^* \zeta_\gamma \tag{7.129}$$

where the dimensionless mass transfer coefficient is defined as $\alpha^* = \dfrac{a l_\beta^2}{D_\beta}$, and l_β is a characteristic length of the β-phase. Then, in dimensionless notation, the boundary value problems read as follows: In the β-phase:

$$Pe_\beta \mathbf{v} \cdot \nabla \zeta_\beta = \nabla^2 \zeta_\beta - \varepsilon_\beta^{-1} \tag{7.130}$$

$$\mathbf{n}_{\beta\sigma} \cdot \nabla \zeta_\beta = 0 \quad \text{at} \quad A_{\beta\sigma} \tag{7.131}$$

where $Pe_\beta = \dfrac{\langle \mathbf{v} \rangle^\beta l_\beta}{D_\beta}$. In the γ-phase:

$$0 = \delta \nabla^2 \zeta_\gamma + \varepsilon_\gamma^{-1} \tag{7.132}$$

$$\mathbf{n}_{\gamma\sigma} \cdot \nabla \zeta_\gamma = 0 \quad \text{at} \quad A_{\gamma\sigma} \tag{7.133}$$

$$\langle \zeta_\gamma \rangle = 0 \tag{7.134}$$

where $\delta = \frac{D_\gamma}{D_\beta}$. The two problems are coupled at their interface through the condition:

$$\zeta_\beta = \frac{1}{K}\zeta_\gamma \quad \text{at } A_{\beta\gamma} \tag{7.135}$$

In this notation, the mass transfer coefficient becomes:

$$\alpha^* = -\frac{\varepsilon_\beta}{\langle \zeta_\beta \rangle} \tag{7.136}$$

One final substitution will allow for additional insight. Define:

$$\phi_\beta = \delta K \varepsilon_\gamma \zeta_\beta \tag{7.137}$$

and

$$\phi_\gamma = \delta \varepsilon_\gamma \zeta_\gamma \tag{7.138}$$

Then, the two boundary value problems take the canonical form:

$$\mathbf{Pe}_\beta \mathbf{u} \cdot \nabla \phi_\beta = \nabla^2 \phi_\beta - \Lambda \text{ in the} \beta - \text{phase} \tag{7.139}$$

$$\mathbf{n}_{\beta\sigma} \cdot \nabla \phi_\beta = 0 \quad \text{at } A_{\beta\sigma} \tag{7.140}$$

where $\Lambda = \frac{\delta K \varepsilon_\gamma}{\varepsilon_\beta}$ and

$$0 = \nabla^2 \phi_\gamma + 1 \text{ in the } \gamma - \text{phase} \tag{7.141}$$

$$\mathbf{n}_{\gamma\sigma} \cdot \nabla \phi_\gamma = 0 \quad \text{at } A_{\gamma\sigma} \tag{7.142}$$

$$\phi_\beta = \phi_\gamma \quad \text{at } A_{\beta\gamma} \tag{7.143}$$

$$\langle \phi_\gamma \rangle = 0 \tag{7.144}$$

The mass-transfer coefficient is simply:

$$\alpha^* = -\frac{\delta K \varepsilon_\beta \varepsilon_\gamma}{\langle \phi_\beta \rangle} \tag{7.145}$$

7.5.4 Results and Discussion

The above scaling relations are checked against analytical solutions and numerical simulations below. Two different unit cell geometries are used: the first involving two parallel phases of infinite extent, and the second involving a unit cube with a disordered phase distribution.

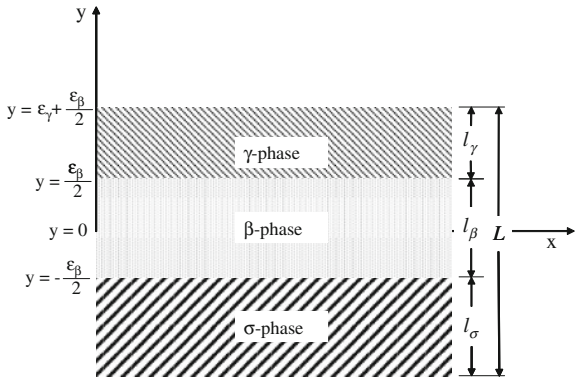

Fig. 7.31 A two-dimensional unit-cell for parallel phases

In the numerical simulations, the velocity field was computed numerically by solving the Stokes equations:

$$\nabla p = \mu \nabla^2 \mathbf{v} \tag{7.146}$$

$$\nabla \cdot \mathbf{v} = 0 \tag{7.147}$$

$$\mathbf{v} = \mathbf{0} \quad \text{at} A_{\beta\sigma} \tag{7.148}$$

where v, p, and μ are the velocity vector, pressure field and fluid viscosity, respectively. The procedure for solving the three-dimensional Stokes flow problem involves discretization in terms of cubic elements and was presented in Sect. 3.5. To numerically solve the transport boundary value problems, a non-uniform finite differences scheme with upwinding was used for discretization, with the resulting linear systems of equations solved again using Successive Over-Relaxation method (SOR).

The solution for simplified geometry of parallel phases assuming one-dimensional flow is presented first. In addition, it is considered that diffusion is significant only in the direction perpendicular to flow. These assumptions correspond to a Pe-independent Type II closure problem similar to that of Quintard and Whitaker [82] for sufficiently fast diffusion. The unit cell is shown Fig. 7.31 and was used to calculate properties of the Taylor-Aris dispersion problem for a passive tracer.

The boundary value problem can be solved analytically in this geometry, yielding the following expression for the dimensionless mass transfer coefficient:

$$\alpha^* = \frac{\varepsilon_\beta \varepsilon_\gamma}{A_1 + A_2 + A_3} \tag{7.149}$$

where the length L of the unit cell is used as characteristic length. (Note that in this notation $\alpha^* = \alpha^\wedge \left(\frac{l_\beta}{L}\right)^2$). The coefficients are, respectively:

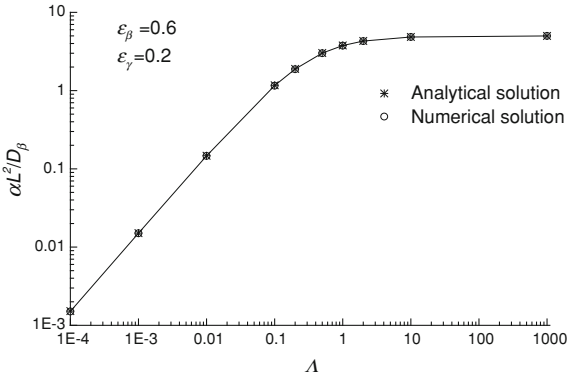

Fig. 7.32 Analytical and numerical results of the dimensionless mass transfer coefficient for parallel phases

$$A_1 = -\frac{1}{6\Lambda}\left[\left(\frac{\varepsilon_\beta}{2}+\varepsilon_\gamma\right)^3 - \frac{\varepsilon_\beta^3}{8}\right]\varepsilon_\beta^2 \tag{7.150}$$

$$A_2 = \frac{1}{2\Lambda}\left(1+\frac{\varepsilon_\beta}{2\varepsilon_\gamma}\right)\left[\left(\frac{\varepsilon_\beta}{2}+\varepsilon_\gamma\right)^2 - \frac{\varepsilon_\beta^2}{4}\right]\varepsilon_\gamma\varepsilon_\beta^2 \tag{7.151}$$

$$A_3 = \frac{\varepsilon_\beta^4\varepsilon_\gamma}{3} - \left(\varepsilon_\gamma+\frac{\varepsilon_\beta}{4}\right)\frac{\varepsilon_\beta^3\varepsilon_\gamma}{2\Lambda} \tag{7.152}$$

In the limiting case of infinitely fast diffusion in the γ-phase ($\delta \to \infty \Rightarrow \Lambda \to \infty$), the asymptotic results are $A_1 \to 0$, $A_2 \to 0$ and $A_3 \to \frac{\varepsilon_\beta^4\varepsilon_\gamma}{3}$, thus the dimensionless mass transport coefficient is $\hat{\alpha} \to \frac{3}{\varepsilon_\beta}$. This result coincides with the analytical mass transport coefficient for parallel phases found by Quintard and Whitaker [82] and shown to be independent of Peclet number.

Figure 7.32 shows the dimensionless mass transfer coefficient plotted as a function of the governing dimensionless parameter $\Lambda = \frac{\delta K \varepsilon_\gamma}{\varepsilon_\beta}$, calculated using both the analytical approach and numerical simulation. The analytical and numerical solutions are almost identical. For low values of Λ, the mass transfer coefficient increases with Λ (i.e. with increasing values of δ and/or K) in a linear fashion. At higher values, α reaches a constant value and becomes practically independent of Λ. The spatial distribution of the dimensionless scalar s_β is shown in Fig. 7.33. In the limiting case of $\Lambda \to \infty \Rightarrow \delta \to \infty$ the calculated s_β values are identical to those found by Quintard and Whitaker [82] for fast diffusion in the γ-phase with the same geometry.

Further investigation of the validity of the asymptotic scaling results in this case, is portrayed in Fig. 7.34, where the dimensionless mass transfer coefficient is plotted against Λ for various values of the fraction ε_β, with the ratio $\frac{\varepsilon_\beta}{\varepsilon_\gamma}$ kept constant.

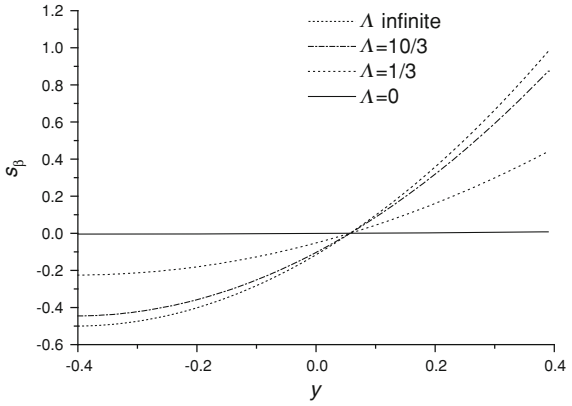

Fig. 7.33 Numerical results for s_β for parallel phases

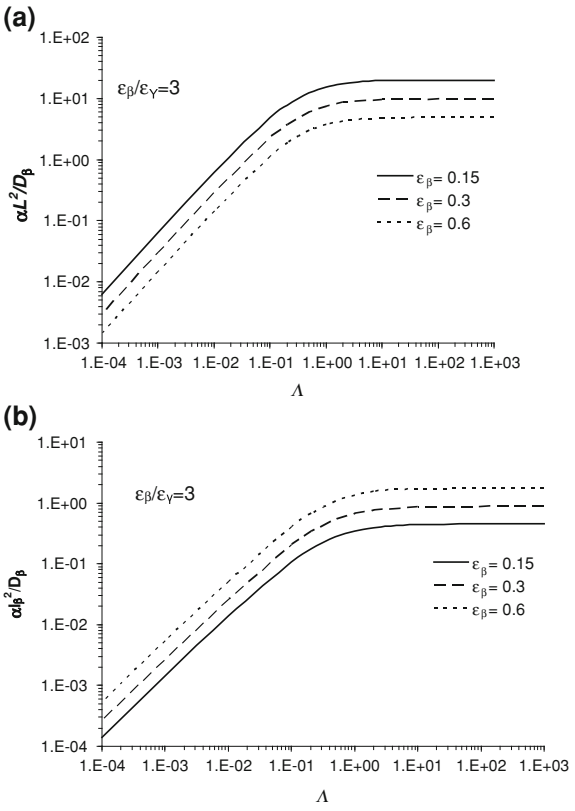

Fig. 7.34 The effect of Λ on the mass transfer coefficient, defined based either on the characteristic length L (**a**) or the characteristic length l_β (**b**) for various values of the volume fraction and for parallel phases. Static conditions

In Fig. 7.34a, the length of the cell, $L = l_\sigma + l_\beta + l_\gamma$, is used as the characteristic length. The mass transfer coefficient $\hat{\alpha}$is shown to decrease linearly with ε_β. This result is in accordance with previous investigations (e.g. see Eq. 47e in [82]) although α^* is expected to increase linearly with ε_β. The explanation lies in the

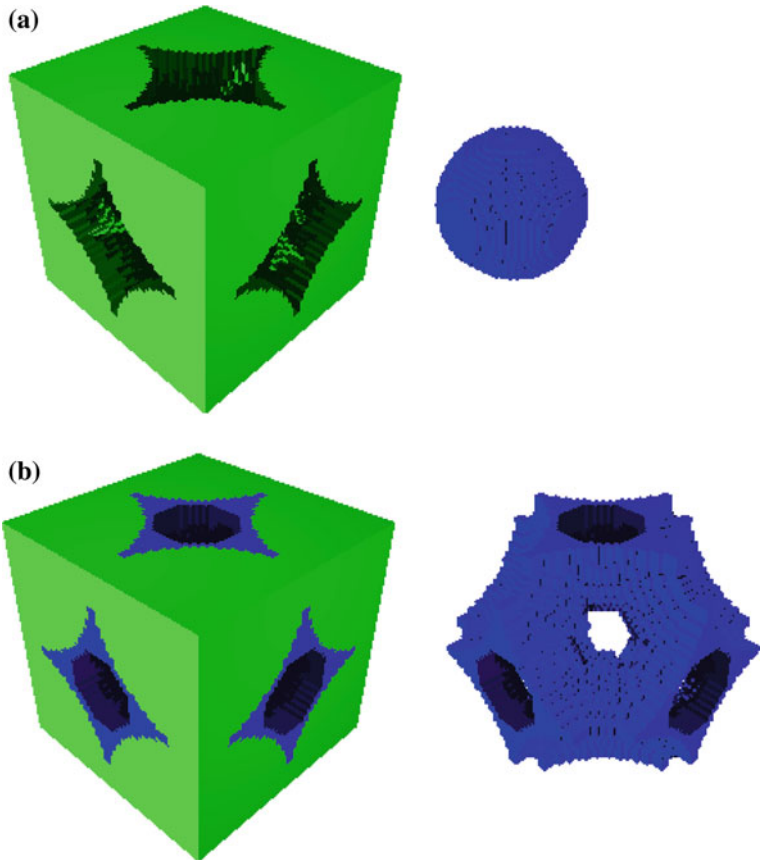

Fig. 7.35 A typical three-dimensional unit cell with the immobile fluid phase configuration in the form of (**a**) blobs, or (**b**) films. Volume fractions are $\varepsilon_\beta = 0.31$, $\varepsilon_\gamma = 0.12$. The immobile phase is also plotted separately for clarity

different characteristic lengths used to non-dimensionalize the mass transfer coefficient. It is not difficult to show that for parallel phase geometry it is $\frac{l_\beta}{L} = \varepsilon_\beta$, hence $\alpha^* = \hat{a}\varepsilon_\beta^2$. Thus, Fig. 7.34b shows the corresponding plot for α^* for various values of ε_β. Where $a^* \to 3\varepsilon_\beta$ when $\delta \to \infty \Leftrightarrow \Lambda \to \infty$, as expected.

More realistic geometries are considered in Fig. 7.35 where a typical periodic three-dimensional unit cell is shown, assumed to represent regularly packed granular porous media.

The solid grains (σ-phase) are located on the eight edges of the cell. For the immobile γ-phase, two different cases are considered:

- The immobile phase does not wet the solid, hence it is distributed in the pore space in the form of blobs.
- The immobile phase wets the solid, hence it is distributed in the pore space in the form of films.

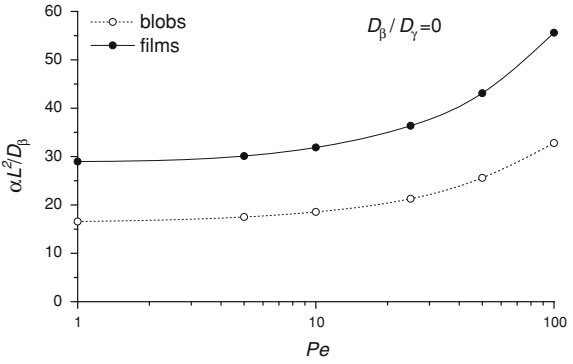

Fig. 7.36 The effect of Peclet number on the mass transfer coefficient for the limiting case of sufficiently fast diffusion in the γ-phase for the three-dimensional unit cell of Fig. 7.35

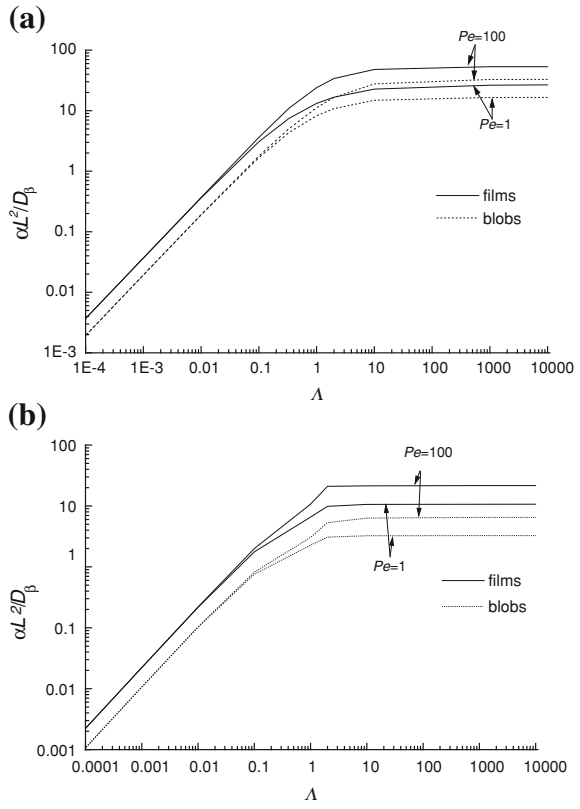

Fig. 7.37 The effect of Peclet number on the curve of the mass transfer coefficient as a function of Λ. Two values are shown, one low (Pe = 1) and another high (Pe = 100). Three dimensional unit cells with volume fractions of (**a**) $\varepsilon_\beta = 0.31$ and $\varepsilon_\gamma = 0.12$, and (**b**) $\varepsilon_\beta = 0.39$ and $\varepsilon_\gamma = 0.04$

In both cases the "aqueous" phase (β-phase) flows under Stokes flow conditions. Initially, the case of infinitely fast diffusion in the γ-phase $\left(\delta = \dfrac{D_\gamma}{D_\beta} \to \infty\right)$ is considered. The effect of the pore-scale Peclet number on the dimensionless mass transfer coefficient is shown in Fig. 7.36 for $\delta \to \infty$.

The mass transfer coefficient is nearly constant at low Peclet numbers (of the order of less than unity), and starts increasing when the Peclet number increases. The wetting condition affects the value of the mass transfer coefficient: the film (wetting) configuration of the immobile phase yields mass transfer coefficients always larger than those corresponding to blobs (non-wetting). This is a result of the higher surface area per unit volume available in films compared to those of blobs for the same volumetric fractions. In addition, it should be noted that these results are in excellent agreement with the theoretical investigation of Ahmadi et al. [6].

In Fig. 7.37, the effect of the dimensionless parameter Λ on the mass transfer coefficient is shown for two different values of Peclet number. Again, the mass transport coefficient increases linearly with Λ at low Λ values, and reaches a constant value at high Λ. As before, the mass transfer coefficient is higher when the immobile phase is wetting (films) rather than non-wetting (blobs). The coefficient is independent of the Peclet number for low Λ values. When ε_β and ε_γ vary, the resulting trends are qualitatively similar, as observed by comparing Fig. 7.37a, b. It is important to note that in these simulations, the dry porosity remains constant and equal to 0.43, ε_γ varied from 0.12 to 0.4 and, consequently, ε_β varied from 0.31 to 0.39. It is evident that as ε_γ decreases so does the mass transfer coefficient.

References

1. Achenbach, E., Reinsche, E.: Methane/steam reforming kinetics for solid oxide fuel cells. J. Power Sources **52**, 238–299 (1994)
2. Adler, P.M., Jacquin, C.J., Quiblier, J.A.: Flow in simulated porous media. Int. J. Multiphase Flow **16**, 691–712 (1990)
3. Agterof, W.G.M., Vaessen, G.E.J., Haagh, G.A.A.V., Klahn, J.K., Janssen, J.J.M.: Prediction of emulsion particle sizes using a computational fluid dynamics approach. Colloid Surf. B **31**, 141–148 (2003)
4. Aguiar, P., Adjimana, C.S., Brandona, N.P.: Anode-supported intermediate temperature direct internal reforming solid oxide fuel cell. I: model-based steady-state performance. J. Power Sources **138**, 120–136 (2004)
5. Ahmadi, A., Quintard, M., Whitaker, S.: Transport in chemically and mechanically heterogeneous porous media V: two-equation model for solute transport with adsorption. Adv. Water Resour. **22**, 59–86 (1998)
6. Ahmadi, A., Aigueperse, A., Quintard, M.: Calculation of the effective properties describing active dispersion in porous media: from simple to complex porous media. Adv. Water Resour. **24**, 423–438 (2001)
7. Ahmed, K., Foger, K.: Kinetics of internal steam reforming of ethane on Ni/YSZ based anodes for solid oxide fuel cells. Catal. Today **63**, 479–487 (2000)
8. Alves, M.A., Delgado, J.M.P.Q., Guedes de Carvalho, J.R.F.: Mass transfer from cylinders and plane surfaces buried in packed beds in alignment with the flow direction. Chem. Eng. Sci. **61**, 1174–1183 (2006)
9. Bekri, S., Thovert, J.F., Adler, P.M.: Dissolution and deposition in fractures. Eng. Geol. **48**, 283–308 (1997)
10. Bekri, S., Adler, P.M.: Dispersion in multiphase flow through porous media. Int. J. Multiphase Flow **28**, 665–697 (2002)

11. Bird, R.B., Stewart, W., Lightfoot, E.N.: Transport Phenomena. Wiley, New York (1960)
12. Bomberg, M.: Moisture flow through porous building materials. In: Report no. 52, Division of Building Technology, Lund Institute of Technology, Lund, Sweden (1974)
13. Bravo, M.C., Araujoc, M., Lago, M.: Pore network modeling of two-phase flow in a liquid-(disconnected) gas system. Physica A **375**, 1–17 (2007)
14. Carbonell, R.G., Whitaker, S.: Heat and mass transfer in porous media. In: Bear, J., Carpacioglu, M.Y. (eds.) Fundamentals of Transport Phenomena in Porous Media. Martinus Nijhoff Publ, Dordrecht (1984)
15. Chesters, A.K.: The modeling of coalescence processes in fluid-liquid dispersions. Chem. Eng. Res. Des. **69**, 259–270 (1991)
16. Coelho, M.A.N., Guedes de Carvalho, J.R.F.: Transverse dispersion in granular beds: Part II–mass transfer from large spheres immersed in fixed or fluidised beds of small inert particles. Chem. Eng. Res. Des. **66**, 178–189 (1988)
17. Colombert, R.: L'Humidité des bâtiments anciens; causes et effets; Diagnostic et remèdes, Editions du Moniteur, Paris (1975)
18. Costa-Nunes, O., Gorte, R.J., Vohs, J.M.: Comparison of the performance of Cu-CeO_2-YSZ and Ni-YSZ composite SOFC anodes with H_2, CO and syngas. J. Power Sources **141**, 241–249 (2005)
19. Costamagna, P., Magistri, L., Massardo, A.F.: Design and part-load performance of a hybrid system based on a solid oxide fuel cell reactor and a micro gas turbine. J. Power Sources **96**, 352–368 (2001)
20. Coutelieris, F.A., Kainourgiakis, M.E., Stubos, A.K.: Low Peclet mass transport in assemblages of spherical particles for two different adsorption mechanisms. J. Colloid Interface Sci. **264**, 20–29 (2003)
21. Crank, J.: The mathematics of diffusion, 2nd edn. Oxford University Press, UK (1975)
22. Dagan, G., Lessoff, S.: Solute transport in heterogeneous formations of bimodal conductivity distribution: 1. Theory. Water Resour. Res. **37**, 465–472 (2001)
23. Dullien, F.A.: Porous Media: Fluid Transport and Pore Structure. Academic Press, California (1979)
24. Fenwick, D.H., Blunt, M.: Three-dimensional modeling of three phase imbibition and drainage. Adv. Water Resour. **21**, 121–143 (1998)
25. Ferguson, J.R., Fiard, J.M., Herbin, R.: Three-dimensional numerical simulation for various geometries of solid oxide fuel cells. J. Power Sources **58**, 109–122 (1996)
26. Freitas, V.P., Guimarães, A.S.: Characterization of a hygro-regulated wall base ventilation system for treatment of rising damp in historical buildings. In: Proceedings of the 2nd Nordic Symposium on Building Physics, Copenhagen, Denmark, pp. 911–919 (2008)
27. Fried, J.J., Muntzer, P., Zilliox, L.: Groundwater pollution by transfer of oil-hydrocarbons. Ground Water **17**, 586–594 (1979)
28. Geller, J.T., Hunt, J.R.: Mass transfer from non-aqueous phase organic liquids in water-saturated porous media. Water Resour. Res. **29**, 833–845 (1993)
29. Gerami, S., Pooladi-Darvish, M.: Predicting gas generation by depressurization of gas hydrates where the sharp-interface assumption is not valid. J. Pet. Sci. Eng. **56**, 146–164 (2007)
30. Goldschmidt, M.J.V., Weijers, G.G.C., Boerefijn, R., Kuipers, J.A.M.: Discrete element modelling of fluidised bed spray granulation. Powder Technol. **138**, 39–45 (2003)
31. Guedes de Carvalho, J.R.F., Delgado, J.M.P.Q., Alves, M.A.: Mass transfer between flowing fluid and sphere buried in packed bed of inerts. AIChE J. **50**, 65–74 (2004)
32. Grace, H.P.: Dispersion phenomena in high-viscosity immiscible fluid systems and application of static mixers as dispersion devices in such systems. Chem. Eng. Commun. **14**, 225–277 (1982)
33. Grgicak, C.M., Green, R.G., Giorgi, J.B.: SOFC anodes for direct oxidation of hydrogen and methane fuels containing H_2S. J. Power Sources **179**, 317–328 (2008)

34. Guimarães, A.S., Delgado, J.M.P.Q., de Freitas, V.P.: Mathematical analysis of the evaporative process of a new technological treatment of rising damp in historic buildings. Build. Environ. **45**, 2414–2420 (2010)
35. Gurau, V., Liu, H., Kakac, S.: Two-dimensional model for proton exchange membrane fuel cells. AIChE J. **44**, 2410–2422 (1998)
36. Gummerson, R.J., Hall, C., Hoff, W.D.: Water movement in porous building materials-III. A sorptivity test procedure for chemical injection damp proofing. Build. Environ. **16**, 193–199 (1981)
37. Gvirtzam, H., Paldor, N., Magaritz, M., Bachmat, Y.: Mass exchange between mobile freshwater and immobile saline water in the unsaturated zone. Water Resour. Res. **24**, 1638–1644 (1988)
38. Gwo, J.P., O'Brien, R., Jardine, P.M.: Mass transfer in structured porous media: embedding mesoscale structure and microscale hydrodynamics in a two-region model. J. Hydrol. **208**, 204–222 (1998)
39. Hall, C., Hoff, W.D.: Water transport in brick, stone and concrete. Taylor and Francis, New York (2002)
40. Hall, C., Hoff, W.D.: Rising damp: capillary rise dynamics in walls. Proc. R. Soc. A Math. Phy. **463**, 1871–1884 (2007)
41. He, H., Hill, J.M.: Carbon deposition on Ni/YSZ composites exposed to humidified methane. Appl. Catal. A Gen **317**, 284–292 (2007)
42. Heibel, A.K., Scheenen, T.W.J., Heiszwolf, J.J., van As, H., Kapteijn, F., Moulijn, J.A.: Gas and liquid phase distribution and their effect on reactor performance in the monolith film flow reactor. Chem. Eng. Sci. **56**, 5935–5944 (2001)
43. Hirschenhofer, J.H., Stauffer, D.B., Engleman, R.R., Klett, M.G.: Fuel Cell Handbook, 4th edn. Business/Technology Books, Orinda (1997)
44. Holm, A., Kunzel, H.M.: Two-dimensional transient heat and moisture simulations of rising damp with WUFI-2D. In: Proceedings of the 2nd International Conference on Building Physics, Leuven, Belgium, pp. 363–3677 (2003)
45. Hunt, J.R., Sitar, N., Udell, K.S.: Non-aqueous phase liquid transport and cleanup I: analysis of mechanisms. Water Resour. Res. **24**, 1247–1258 (1988)
46. Inamuro, T.: Lattice Boltzman methods for viscous fluid flows and for two-phase fluid flows. Fluid Dyn. Res. **38**, 641–659 (2006)
47. Irvine, J.T.S., Sauvet, A.: Improved oxidation of hydrocarbons with new electrodes in high temperature fuel cells. Fuel Cells **1**, 205–210 (2001)
48. Jamsak, W., Assabumrungrat, S., Douglas, P.L., Laosiripojana, N., Suwanwarangkul, R., Charojrochkul, S., Croiset, E.: Performance of ethanol-fuelled solid oxide fuel cells: proton and oxygen ion conductors. Chem. Eng. J. **133**, 187–194 (2007)
49. Janssen, J.J.M., Boon, A., Agterof, W.G.M.: Influence of dynamic interfacial properties on droplet break-up in simple shear flow. AIChE J. **40**, 1929–1939 (1994)
50. Jaouen, F., Lindbergh, G., Sundholm, G.: Investigation of mass-transport limitations in the solid polymer fuel cell cathode. J. Electrochem. Soc. **149**, A437–A447 (2002)
51. Kainourgiakis, M.E., Kikkinides, E.S., Stubos, A.K.: Diffusion and flow in porous domains constructed using process-based and stochastic techniques. J. Porous Mat. **9**, 141–154 (2002)
52. Kamp, A.M., Chesters, A.K., Colin, C., Fabre, J.: Bubble coalescence in turbulent flows: a mechanistic model for turbulence-induced coalescence applied to microgravity bubbly pipe flow. Int. J. Multiphase Flow **27**, 1363–1396 (2001)
53. Kay, A.L., Davies, H.N.: Calculating potential evaporation from climate model data: a source of uncertainty for hydrological climate change impacts. J. Hydrol. **358**, 221–239 (2008)
54. Kikkinides, E.S., Burganos, V.N.: Permeation properties of three-dimensional self-affine reconstructions of porous materials. Phys. Rev. E **62**, 6906–6915 (2000)
55. Kim, T., Ahn, K., Vohs, J.M., Gorte, R.J.: Deactivation of ceria-based SOFC anodes in methanol. J. Power Sources **164**, 42–48 (2007)

56. Kimball, B.A., Jackson, R.D., Reginato, R.J., Nakayama, F.S., Idso, S.B.: Comparison of field-measures and calculated soil-heat fluxes. Soil Sci. Soc. Am. Proc. **40**, 18–25 (1976)
57. Klahn, J.K., Janssen, J.J.M., Vaessen, G.E.J., de Swart, R., Agterof, W.G.M.: On the escape process during phase inversion of an emulsion. Colloid Surf. A **210**, 167–181 (2002)
58. Klein, J.M., Bultel, Y., Pons, M., Ozil, P.: Modeling of a solid oxide fuel cell by methane: analysis of carbon deposition. J. Fuel Cell Technol. **7**, 425–434 (2007)
59. Kostoglou, M., Karabelas, A.J.: Evaluation of zero order methods for simulating particle coagulation. J. Colloid Interface Sci. **163**, 420–431 (1994)
60. Kostoglou, M., Karabelas, A.J.: Induced pulsing in trickle beds-characteristics and attenuation of pulses. Chem. Eng. Sci. **60**, 6584–6595 (2005)
61. Kunzel, H.M.: Simultaneous heat and moisture transport in building components; one and two dimensional calculation using simple parameters. Dissertaion, University of Stuttgart (1995)
62. Lam, A.C., Schechter, R.S., Wade, W.H.: Mobilization of residual oil under equilibrium and non-equilibrium conditions. Soc. Petrol. Eng. J. **23**, 781–790 (1983)
63. La O', G.J., In, H.J., Crumlin, E., Barbastathis, G., Shao-Horn, Y.: Recent advances in micro devices for electrochemical energy conversion and storage. Int. J. Energy Res. **31**, 548–575 (2007)
64. Lehr, F., Millies, M., Mewes, D.: Bubble-size distributions and flow fields in bubble columns. AIChE J. **48**, 2426–2443 (2002)
65. Lessoff, S., Dagan, G.: Solute transport in heterogeneous formations of bimodal conductivity distribution: 2. Applications. Water Resour. Res. **37**, 473–480 (2001)
66. Lin, Y.B., Zhan, Z.L., Liu, J., Barnett, S.A.: Direct operation of solid oxide fuel cells with methane fuel. Solid State Ionics **176**, 1827–1835 (2005)
67. Lu, N., Li, Q., Sun, X., Khaleel, M.A.: The modeling of a standalone solid-oxide fuel cell auxiliary power unit. J. Power Sources **1661**, 938–948 (2006)
68. Luo, L.S., Girimaji, S.S.: Lattice Boltzmann model for binary mixtures. Phys. Rev. E **66**, 035301/1–035301/4 (2002)
69. Luo, L.S., Girimaji, S.S.: Theory of the lattice Boltzmann method: two-fluid model for binary mixtures. Phys. Rev. E **67**, 036302/1–036302/11 (2003)
70. Luo, L.S., Svensen, H.F.: Theoretical model for drop and bubble breakup in turbulent dispersions. AIChE **42**, 1225–1233 (1996)
71. Matsuzaki, Y., Baba, Y., Sakurai, T.: High electric conversion efficiency and electrochemical properties of anode-supported SOFCs. Solid State Ionics **174**, 81–86 (2004)
72. Mingzhe, D., Dullien, F., Jun, Z.: Characterization of water-flood saturation profile histories by the 'complete' capillary number. Transp. Porous Media **31**, 213–237 (1998)
73. Mousavi, S.M., Jafari, A., Yaghmaei, S., Vossoughi, M., Sarkomaa, P.: Computer simulation of fluid motion in a porous bed using a volume of fluid method: application in heap leaching. Miner. Eng. **19**, 1077–1083 (2006)
74. Nagel, F.P., Schildhauer, T., Biollaz, S.M.A., Wokaun, A.: Performance comparison of planar, tubular and Delta8 solid oxide fuel cells using a generalized finite volume model. J. Power Sources **184**, 143–164 (2008)
75. Newman, J.S., Tabias, C.W.: Theoretical analysis of current distribution in porous electrodes. J. Electrochem. Soc. **109**, 1183–1191 (1962)
76. Ni, M., Leung, D.Y.C., Leung, M.K.H.: Mathematical modeling of ammonia-fed solid oxide fuel cells with different electrolytes. Int. J. Hydrogen Energy **33**, 5765–5772 (2008)
77. Park, S., Cracium, R., Vohs, J.M., Gorte, R.J.: Direct oxidation of hydrocarbons in a solid oxide fuel cell I. Methane oxidation. J. Electrochem. Soc. **146**, 3603–3605 (1999)
78. Plumb, O.A., Whitaker, S.: Diffusion, adsorption and dispersion in heterogeneous porous media: the method of large scale averaging. In: Cushman, J.H. (ed.) Dynamics of Fluids in Hierarchical Porous Media. Academic Press, New York (1990)
79. Pulkrabek, W.W.: Engineering Fundamentals of the Internal Combustion Engine, 2nd edn. Pearson Prentice Hall, New Jeresey (2003)

80. Quintard, M., Whitaker, S.: One and two equation models for transient diffusion processes in two-phases systems. Adv Heat Transfer **23**, 369–464 (1993)
81. Quintard, M., Whitaker, S.: Transport in ordered and disordered porous media: volume averaged equations, closure problems and comparison with experiments. Chem. Eng. Sci. **48**, 2537–2564 (1993)
82. Quintard, M., Whitaker, S.: Convection, dispersion and interfacial transport of contaminants: homogeneous porous media. Adv. Water Res. **17**, 221–239 (1994)
83. Ramakrishna, P.A., Yang, S., Sohn, C.H.: Innovative design to improve the power density of a solid oxide fuel cell. Power Sources **158**, 378–384 (2006)
84. Riensche, E., Achenbach, E., Froning, D., Haines, M.R., Heidug, W.K., Lokurlu, A., von Andrian, S.: Clean combined-cycle SOFC power plant–cell modelling and process analysis. J. Power Sources **86**, 404–410 (2000)
85. Sheng, J.J., Hayes, R.E., Maini, B.B., Torkite, W.S.: Modelling foamy oil flow in porous media. Transp. Porous Media **35**, 227–258 (1999)
86. Singhal, S.C.: Advances in solid oxide fuel cell technology. Solid State Ionics **135**, 305–313 (2000)
87. Skelland, A.H.P.: Diffusional Mass Transfer. Wiley, New York (1974)
88. de Smedt, F., Wierenga, P.J.: A generalized solution for solute flow in soils with mobile and immobile water. Water Resour. Res. **15**, 1137–1141 (1979)
89. Štěpánek, F., Ansari, M.A.: Computer simulation of granule microstructure formation. Chem. Eng. Sci. **60**, 4019–4029 (2005)
90. Stone, H.A.: Dynamics of drop deformation and break up in viscous fluids. Annu. Rev. Fluid Mech. **26**, 65–102 (1994)
91. Sukeshini, A.M., Habibzadeh, B., Becker, B.P., Stoltz, C.A., Eichhorn, B.W., Jackson, G.S.: Electrochemical oxidation of H_2, CO and CO/H_2 mixtures on patterned Ni anodes on YSZ electrolytes. J. Electrochem. Soc. **153**, A705–A715 (2006)
92. Suwanwarangkul, R., Croiset, E., Pritzker, M.D., Fowler, M.W., Douglas, P.L., Entchev, E.: Modelling of a cathode-supported tubular solid oxide fuel cell operating with biomass-derived synthesis gas. J. Power Sources **166**, 386–399 (2007)
93. Torres, M.I.M., Freitas, V.P.: Treatment of rising damp in historical buildings: wall base ventilation. Build. Environ. **42**, 424–435 (2007)
94. Tseronis, K., Kookos, I.K., Theodoropoulos, C.: Modelling mass transport in solid oxide fuel cells anodes: a case for multicomponent dusty gas model. Chem. Eng. Sci. **63**, 5626–5638 (2008)
95. Tsipis, E.V., Kharton, V.V.: Electrode materials and reaction mechanisms in solid oxide fuel cells: a brief review II. Electrochemical behavior vs. materials science aspects. J. Solid State Electrochem. **12**, 1367–1391 (2008)
96. Vogel, T., Gerke, H., Zhang, R., Ge-nuchten, M.V.: Modeling flow and transport in a two-dimensional dual-permeability system with spatially variable hydraulic properties. J. Hydrol. **238**, 78–89 (2000)
97. Walters, K.M., Dean, A.M., Zhu, H.Y., Kee, R.J.: Homogeneous kinetics and equilibrium predictions of coking propensity in the anode channels of direct oxidation solid-oxide fuel cells using dry natural gas. J. Power Sources **123**, 182–189 (2003)
98. Wang, T., Wang, J., Jin, J.: A novel theoretical breakup kernel function of bubble/droplet in a turbulent flow. Chem. Eng. Sci. **59**, 2593–2595 (2003)
99. Watt, D., Colston, B.: Investigating the effects of humidity and salt crystallization on medieval masonry. Build. Environ. **35**, 737–749 (2000)
100. Wexler, E.J.: Analytical solutions for one-, two-, and three-dimensional solute transport in ground-water systems with uniform flow. In: U.S. Geological Survey Techniques of Water-Resources Investigations, Book 3, Chap. B7, p. 190 (1992)
101. Wieringa, J.A., van Dieren, F., Janssen, J.J.M., Agterof, W.G.M.: Droplet break-up mechanism during emulsification in colloid mills at high dispersed fraction. Inst. Chem. Eng. **74**, 554–562 (1996)
102. Whitaker, S.: Diffusion and dispersion in porous media. AIChE J. **13**, 420–427 (1967)

103. Whitaker, S.: Simultaneous heat, mass and momentum transfer in porous media: A theory of drying. Adv. Heat Transf. **13**, 119–203 (1977)
104. Xu, J., Froment, G.F.: Methane steam reforming and water-gas shift: I intrinsic kinetics. AIChE J. **35**, 88–96 (1989)
105. Zanotti, F., Carbonell, R.G.: Development of transport equations for multiphase systems I: general development for two-phase systems. Chem. Eng. Sci. **39**, 263–278 (1984)
106. Zanotti, F., Carbonell, R.G.: Development of transport equations for multiphase systems II: application to one-dimensional axi-symmetric flows of two-phases. Chem. Eng. Sci. **39**, 279–297 (1984)
107. Zhu, H., Kee, R.J., Pillai, M.R., Barnett, S.A.: Modeling electrochemical partial oxidation of methane for cogeneration of electricity and syngas in solid–oxide fuel cells. J. Power Sources **183**, 143–150 (2008)